

# JOINT AND INDIVIDUAL ANALYSIS OF BREAST CANCER HISTOLOGIC IMAGES AND GENOMIC COVARIATES

BY IAIN CARMICHAEL\*, BENJAMIN C. CALHOUN<sup>†</sup>, KATHERINE A. HOADLEY<sup>†</sup>, MELISSA A. TROESTER<sup>†</sup>, JOSEPH GERADTS<sup>‡</sup>, HEATHER D. COUTURE<sup>§</sup>, LINNEA OLSSON<sup>†</sup>, CHARLES M. PEROU<sup>†</sup>, MARC NIETHAMMER<sup>†</sup>, JAN HANNIG<sup>†</sup>, AND J.S. MARRON<sup>†</sup>

*University of Washington\**, *University of North Carolina at Chapel Hill<sup>†</sup>*, *City of Hope National Medical Center<sup>‡</sup>*, and *Pixel Scientia Labs<sup>§</sup>*

A key challenge in modern data analysis is understanding connections between complex and differing modalities of data. For example, two of the main approaches to the study of breast cancer are histopathology (analyzing visual characteristics of tumors) and genetics. While histopathology is the gold standard for diagnostics and there have been many recent breakthroughs in genetics, there is little overlap between these two fields. We aim to bridge this gap by developing methods based on Angle-based Joint and Individual Variation Explained (AJIVE) to directly explore similarities and differences between these two modalities. Our approach exploits Convolutional Neural Networks (CNNs) as a powerful, automatic method for image feature extraction to address some of the challenges presented by statistical analysis of histopathology image data. CNNs raise issues of interpretability that we address by developing novel methods to explore visual modes of variation captured by statistical algorithms (e.g. PCA or AJIVE) applied to CNN features. Our results provide many interpretable connections and contrasts between histopathology and genetics.

**1. Introduction.** The era of big data is marked not only by large datasets, but also complex modalities of data such as images, networks, and text. A key challenge in the analysis of complex data is data representation: what do you measure to capture the signal of interest (Marron and Alonso, 2014)? Automated, data-driven methods for feature extraction have proven to be powerful tools for analyzing complex data (Bengio, Courville and Vincent, 2013). This is particularly true for predictive problems involving data modalities such as images and text where deep learning has made major advances. Developing *interpretable*, data-driven feature extraction methods – particularly for inferential analyses where the goal is for humans to learn about the underlying signal – is an ongoing challenge (Doshi-Velez and Kim, 2017; Olah et al., 2018).

Modern scientific applications increasingly involve relating *multiple* modalities of data to one another. The *multi-block* data setting<sup>1</sup> means a fixed set of observations (e.g. patients) and several sets of variables (e.g. gene expression, copy number, protein). The classical example of a multi-block data algorithm is *canonical correlation analysis* (CCA) which, given two data blocks, estimates a low dimensional *joint signal* capturing the information shared by the two blocks (Hotelling, 1936). The multi-block data setting arises in recent cancer studies such as the Cancer Genome Atlas (Network et al., 2012).

---

*MSC 2010 subject classifications:* Primary 62H35, 62P10

*Keywords and phrases:* Multi-view data, dimensionality reduction, image analysis, deep learning, interpretability, breast cancer histopathology, gene expression

<sup>1</sup>This setting is also referred to as *multi-view*, *multi-modal*, or *multi-omic* data. Related terms include *data fusion* and *data integration*.

Two of the main approaches to the study of breast cancer are histopathology and genetics. Pathologic assessment of breast tissue is the current state of the art method for breast cancer diagnosis. A pathologist examines the tissue under a microscope in order to determine if there is cancer as well as to assess important features used for determining the course of treatment including histologic type, invasive status, tumor size, lymph node status, grade, as well as stain for hormone receptors and HER2. Histopathology is the classical approach for diagnosing cancer dating back to the 1800s (Rosen, 2001; Titford, 2006). Figure 1 shows an image of a *hematoxylin and eosin* stained (H&E) breast cancer tumor from the dataset analyzed in this paper. Complementary to histopathology, genetic information is increasingly used to understand the biological processes underlying cancer. Genetics also plays an important role in tumor clustering/classification as well as predicting patient prognosis and response to treatments (Györffy et al., 2015).

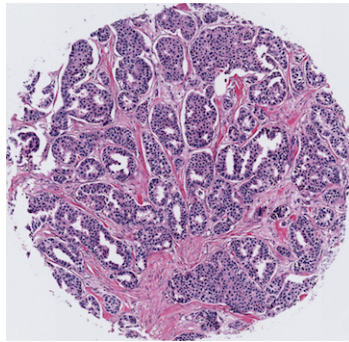


Fig 1: A lower resolution view of a *hematoxylin and eosin* (H&E) stained 1mm core from a breast cancer tissue microarray. The darker purple color (hematoxylin) stains nuclear material such as DNA, while the pink (eosin) highlights structures such as connective tissue.

Most existing research in breast cancer focuses on a single data modality e.g. either histopathology or genetics. For example, the development of automated algorithms to augment human pathologists' judgements using machine learning is active area of research that aims to increase diagnostic accuracy and decrease costs (Liu et al., 2017; Couture et al., 2018; Veta et al., 2019). Subtype discovery (clustering) based on gene expression data is another major area of research (Perou et al., 2000; Parker et al., 2009). Exploratory/inferential analyses, which study direct associations between histopathology and genetics, are receiving increasing interest in recent years, but are hindered by the challenge of doing inferential analysis on image data (Ash et al., 2018).

The Carolina Breast Cancer Study Phase 3 (CBCS) is a cohort of breast cancer survivors diagnosed between 2008 and 2013 and with both histologic and gene expression data (Troester et al., 2017). CBCS provides a unique opportunity to explore both connections and differences between genomics and histopathology that could lead to new discoveries e.g. improved classification. It is known that genetics plays an important role in cancer development, so one might expect to see *joint* modes of variation between the genetic and histopathological data. However, not all information in one data modality is contained in the other, therefore, we expect to also see *histopathology individual* as well as *genetic individual* modes of variation. To estimate these three different kinds of signals, we use *angle-based joint and individual variation explained* (AJIVE) (Feng et al., 2018).

Statistical analysis of images presents difficulties for feature extraction. Convolutional neural networks (CNNs) have proven adept at solving predictive tasks with images (Fukushima, 1980; LeCun, Bengio and Hinton, 2015). Inspired by the approach in Couture et al. (2018), we use an intermediate layer of a pre-trained neural network (see Section 2.2) for automatic image feature extraction – so called *transfer learning* (Yosinski et al., 2014; Sharif Razavian et al., 2014). We

explore the limits of transfer learning and show that pre-trained CNN features with no fine tuning are able to capture complex visual signals in a domain vastly different than the one they were originally trained for. See Section 5.0.2 for a longer discussion of transfer learning in the context of this paper. While the use of CNNs allows us to capture rich visual information, it presents difficulties because neural network features are notoriously difficult to interpret.

Leveraging deep learning for exploratory/inferential tasks, where the goal is to learn about patterns in the data, presents new challenges and is an active area of investigation (Ash et al., 2018; Adebayo et al., 2018; Olah et al., 2018). We develop a multi-scaled approach called *representative patch views* (RPV) to interpret signals in the data captured by multivariate statistical algorithms<sup>2</sup> applied to neural features (Section 3.1). This approach takes a patch-based representation of each H&E image, allowing us to localize regions in each image that play an important role in a given mode of variation. The RPVs operate at both the core level and patch level, providing a pathologist with two different levels of granularity to explore the visual features associated with a particular mode of variation.

Our AJIVE analysis is able to discover clear, interpretable, joint signals such as associations between Basal-like (genetics) and high grade tumors (histology). The analysis also finds clear individual signals in the histopathological data such as fat content and mucinous tumors.

Section 1.1 below discusses the results of the first AJIVE joint component which captures tumor grade from the pathology perspective and the contrast between the Basal-like and Luminal A PAM50 subtypes from the genetic perspective. Section 2 presents the data provided by CBCS as well as the patch based, CNN image features extraction approach. Section 3 discusses the methods used in this paper including the representative patch views and AJIVE. Section 4 interprets the joint, image individual and genetic individual AJIVE components. Finally, Section 5 concludes with more discussion about transfer learning and exploratory analysis with deep learning.

All correlations and AUC statistics reported in the text of the paper are statistically significant at a level of 0.05 after controlling for multiple testing with the Benjamini-Hochberg procedure Benjamini and Hochberg (1995) unless stated otherwise (see Section A.3).

The Appendix provides additional results and discussion. Section A.1 contains a brief description of the tissue structures relevant to this paper. Section A.2 gives diagnostic plots for the AJIVE analysis of the CBCS data. Section A.3 gives additional details of statistical analyses used in the clinical data interpretation methods. The supplementary material includes a number of figures that were excluded from the main body of the paper for brevity. In particular, all representative patch views examined by pathologists are shown in [Supplement A](#).

**1.1. Results of the first AJIVE joint component.** This section discusses the results of the first AJIVE joint component; many of the technical details (e.g. the RPVs and multiple testing control) are provided in Sections 2 and 3. In the CBCS dataset available to us there are  $n = 1191$  subjects,  $d_1 = 50$  genes (the PAM50 gene set) and  $d_2 = 512$  neural network features extracted from the pathology images using a mean pool of the last convolutional layer of VGG16 (Simonyan and Zisserman, 2014). To help interpret the results of the AJIVE analysis we use a variety of additional variables that are provided by CBCS, but are not used in the AJIVE analysis. These include: PAM50 molecular subtypes, histopathological variables (e.g. pathologist determined tumor grade), immunohistochemical variables (e.g. estrogen receptor (ER) and clinical HER2 status), and patient variables (e.g. age).

---

<sup>2</sup>Many statistical methods such as linear regression, PCA and AJIVE provide loadings vectors of neural features (i.e. vectors in neural feature space) that don't immediately tell us humans anything about the underlying biology.

1.1.1. *Methods overview.* Like *principal components analysis* (PCA), AJIVE returns an (ordered) set of components comprised of *scores vectors* and *loadings vectors* (see Sections 3.2). While PCA returns one set of components, AJIVE returns three sets of components when applied to two data blocks: joint, block one (pathology) individual, and block two (genetic) individual. The joint components capture joint signals shared between the two data blocks; the individual components capture signals present in one data block that are not related to the other data block.

For interpretation purposes, we hypothesize that – like PCA components – each AJIVE component discovers a spectrum contrasting interesting aspects of the data (e.g. Basal-like tumors vs. non-Basal-like tumors). Interpreting the results of the AJIVE analysis often involves understanding what biological phenomena are driving such a spectrum. One AJIVE component assigns a number to each subject (the scores) and subjects can be sorted from most negative to most positive. In the following analysis we consider the *negative* and *positive* extremes of each component.

By exploiting a patch based representation of the images, we can use the AJIVE neural network loadings vectors to create the RPVs which are discussed in detail in Section 3.1 (see Figure 8). Each RPV corresponds to a subject-component-end triple; one subject and one end of one AJIVE component (e.g. subject 12 and the negative end of the first AJIVE joint component). The image patches selected in the RPV are meant to be representative of the visual patterns characteristic of an end of a component. For the sake of exposition, we primarily show a smaller version of the RPVs in the body of the paper, which display only the top 8 patches (e.g. Figure 2).

1.1.2. *Interpretation.* We initially consider the negative and positive extremes of the first joint component separately.

From the pathology perspective, two distinct visual patterns show up in the negative end of the first joint component (Figures 2 and 3). Section A.1 has a brief explanation of the various tumor structures which are relevant to this paper. The first pattern is dense *tumor infiltrating lymphocytes* (TILs) and is illustrated in Figure 2 which shows the RPV of the most negative subject of the first joint component. The smaller cells which have hyperchromatic round nuclei and relatively scant cytoplasm (i.e dark, round, purple structures), are lymphocytes. In particular types of breast cancer, TILs in the intratumoral stroma are associated with prognosis and may be associated with response to immunomodulatory therapy (Wein et al., 2017).

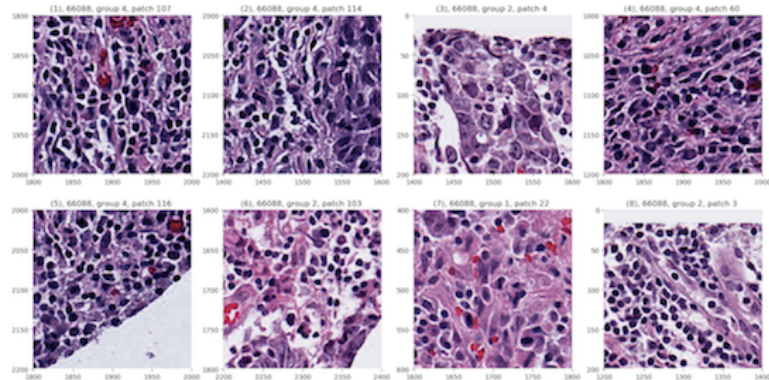


Fig 2: Several representative patches from the most negative subject of joint component 1. The dark, round, purple structures are lymphocyte nuclei; these patches show dense tumor infiltrating lymphocytes which are characteristic of high central grade tumors. The third images in both rows show a significant number of tumor cells, mixed with some lymphocytes. This tumor is a genetically Basal-like tumor like most of the other tumors on the negative end of this component (Figure 5b).

The second visual pattern in the negative end of the first joint component is dense, *high nuclear grade tumor cells* and is illustrated in Figure 3. Nuclear grade describes how abnormal the tumor cells look: “low grade” means the tumor cells look similar to regular cells (“well-differentiated”) and “high grade” means the tumor cells look markedly abnormal (“poorly-differentiated”) e.g. are enlarged and irregularly shaped (Rosen, 2001).

On the positive end of the first joint component, the pathology review shows subjects whose cores contain mostly normal breast tissue i.e. little tumor tissue. This pattern is illustrated by Figure 4, which shows the subject with the most positive scores for the first joint component. These patches contain few tumor cells and are mostly normal breast structures such as *collagenous stroma* (the light pink, stringy tissue) and ducts.

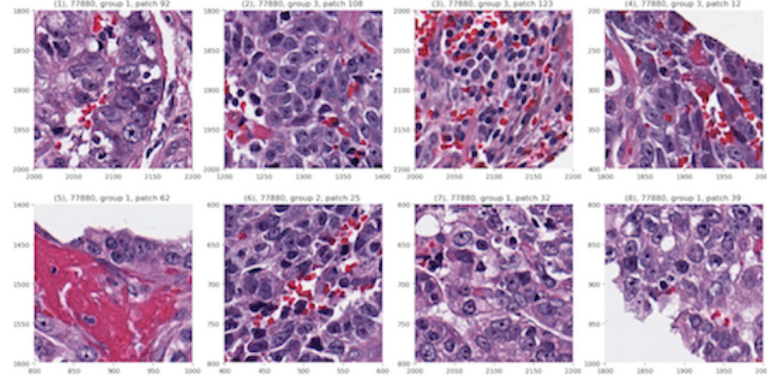


Fig 3: The third most negative subject from joint component 1. The patches selected for the RPV of this tumor show high nuclear grade cells which are large and irregularly shaped. These are also characteristic of high grade tumors. This tumor is also genetically Basal-like.

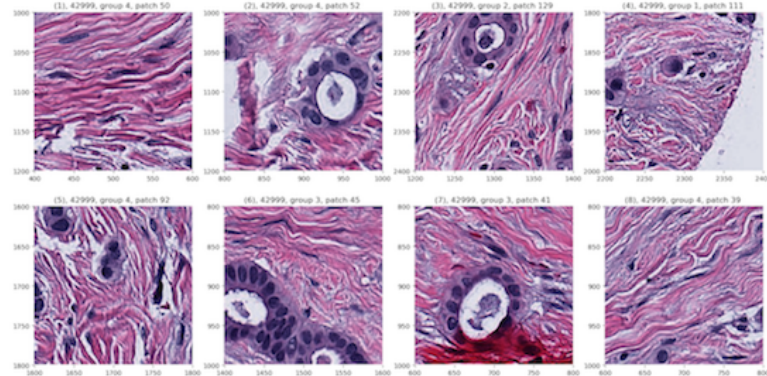
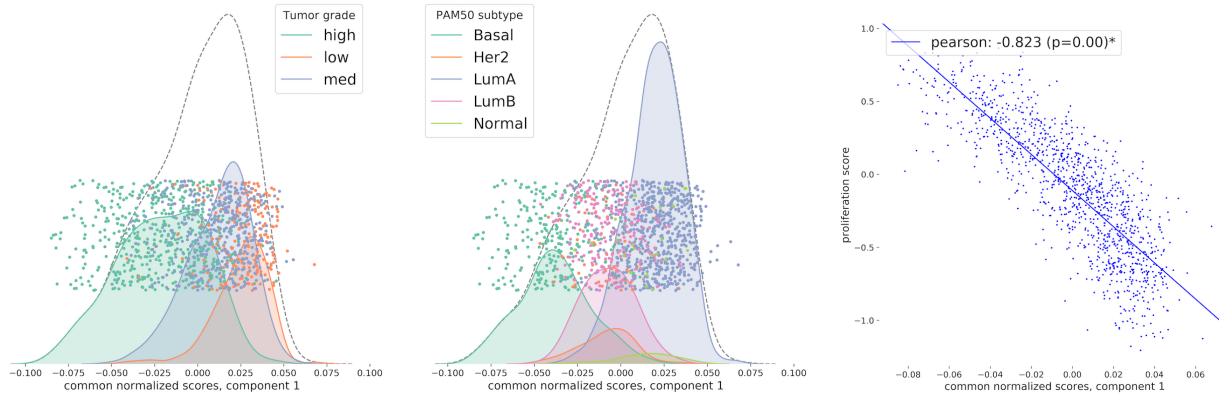


Fig 4: The subject with the most positive scores. These RPV patches are comprised primarily of normal breast tissue and contain few tumor cells. The eosinophilic, fibrillar (light pink, stringy) tissue is collagenous stroma which is found in normal breast tissue while the white circles surrounded by purple dots are neoplastic ducts. This tumor is genetically Luminal A.

The first joint component is related to histopathological features including *tumor grade* and *histological type* (ductal vs. lobular). For example, Figure 5a shows that high *grade* tumors cluster on the negative end of the first joint component while low grade tumors cluster on the positive end (AUC = 0.945). Tumor grade incorporates cellular differentiation and other architectural features

as an indicator of aggressiveness (Elston and Ellis, 2002). This first component is also statistically significantly related to histological type with *ductal* on the negative end and *lobular* on the positive end (AUC = 0.785).



(a) Tumors on the negative end tend to be high grade while those on positive end tend to be low grade.

(b) The Basal-like class is on the negative end of the scores, the HER2/Luminal B classes are in the middle and the Normal/Luminal A classes are on the positive end.

(c) Proliferation score is strongly associated with the common normalized scores with a Pearson correlation of -0.82.

Fig 5: Joint component 1 scores vs. PAM50 molecular subtype (5b), central grade (5a) and proliferation score (5c). The x-axis in each plot shows the subjects' common normalized scores. These figures tell a complementary story. For example, Basal-like tumors tend to be more aggressive, high grade and have a high proliferation score.

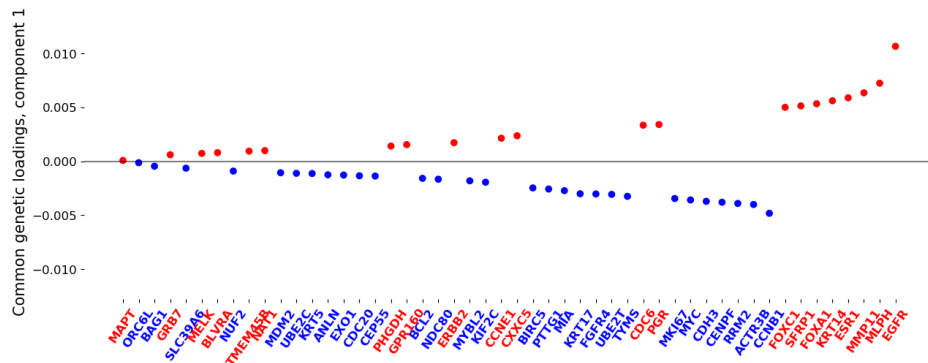


Fig 6: PAM50 loadings vector from joint component 1. Several of the top negative genes are associated with high tumor cellularity and typically have low expression levels in normal breast tissue (consistent with Figures 3 and 2). Several of the top positive genes tend to have high expression levels in normal breast tissue (consistent with Figure 4).

From the genetics perspective, the first joint component strongly tracks the *proliferation score* as well as the contrast between Basal-like vs. Luminal A tumors. Figure 6 shows the PAM50 joint loadings vector for the first component. Several of the top negative genes (e.g. CCNB1, CENPF, MYC, MKI67) are associated with high tumor cell proliferation and tend to have low expression

levels in normal breast tissue. Several of the top positive genes (e.g. MLPH, MMP11) tend to have high expression levels in normal breast tissue. Note that FOXC1 is highly expressed in both basal-like and normal-like breast myoepithelium.

Figure 5b shows that Basal-like tumors cluster on the negative end of the first joint component, molecular HER2 and Luminal B cluster in the middle while Luminal A and normal tumors cluster on the positive end. Note the AUC score for Basal-like vs. Lum A is 0.984 which is quite high. Luminal B and molecular HER2 are separated from Basal-like (AUCs of 0.886 and 0.876). The separation indicates that this joint component is distinguishing more subtle histopathological and molecular features beyond proliferation and cellularity. Figure 5c shows a strong, negative correlation between the first joint component scores and the *proliferation score*, which is a genetic measure indicative of how fast tumor cells grow (Whitfield et al., 2002).

Strikingly, the first joint component almost perfectly separates ROR-PT, which is a combined genetic and pathology based *risk of recurrence score* Parker et al. (2009). Patients with high ROR-PT are clustered on the negative end while patients with a low ROR-PT are clustered on the positive end with an AUC of 0.999.

In addition to genetic phenotypes measured by RNA expression data as just discussed, we also have immunohistochemistry (IHC) data, a surrogate measure of RNA subtypes and the most common way of classifying tumors in a clinical setting. From the IHC perspective, the first joint component is strongly related to ER status and weakly related to clinical HER2 status (see Table 2). Clinical ER negative tumors cluster on the negative end of this component with an AUC of 0.883.

In this first joint component, the pathology and genetics tell complementary stories that are familiar to breast cancer experts. The data raise the possibility that this joint component separates tumors based on one or more histologic features associated with tumor grade. These features could include aspects of nuclear atypia (i.e increased nuclear size, irregular shape, altered chromatin pattern, multiple nucleoli) which are reflected in the nuclear grade. Tumors with a high combined histologic grade also tend to be more cellular and show less tubule or gland formation as compared to low-grade tumors.

From the genetics perspective, Basal-like tumors are on the negative end, molecular HER2/Luminal B tumors are in the middle, and Luminal A/Normal like tumors are on the positive end. The joint scores are strongly negatively correlated with the proliferation score. The negative genes in Figure 6 are predominantly proliferation regulated genes; however, we note several of the positive genes are often considered basal-specific genes. These genes are also expressed in normal myoepithelium and are representative of the normal ducts still observed within slides of the low grade tumors (Livasy et al., 2006; Heng et al., 2017).

Aggressive tumors tend to have high tumor cellularity and little benign tissue. In less aggressive tumors, there is typically more normal breast tissue. Basal-like tumors tend to be more aggressive and are generally associated with high tumor grade, ER negativity, ductal histology, and high proliferation score (Livasy et al., 2006; Troester et al., 2017; Williams et al., 2019). Luminal B and molecular HER2 tumors tend to be moderately aggressive. Luminal A and Normal like tumors are less aggressive and it is known these tend to be low grade.

It is promising that this mode of variation turned up in the first joint component. These connections between the underlying genetic drivers and the pathological impressions have both geneticists and pathologists excited about the potential of AJIVE to quantitatively integrate these different aspects of cancer.

**1.2. Related literature.** There is a large literature on dimensionality reduction for multi-block data including classical algorithms such as CCA Hotelling (1936) and partial least squares Wold (1985) as well as more modern methods such as: multi-block versions of CCA Kettenring (1971);

Nielsen (2002); Asendorf (2015), iNFM Yang and Michailidis (2015), SLIDE Gaynanova and Li (2017) and BASS (Zhao et al., 2014). JIVE Lock et al. (2013) and AJIVE Feng et al. (2018) are some of the first methods to look at both joint as well as individual modes of variation.

Interpretability in deep learning is a growing field (Vellido, Martín-Guerrero and Lisboa, 2012; Molnar et al., 2018; Chen et al., 2018a; Kim et al., 2018; Olah et al., 2018; Holzinger et al., 2019). *Saliency maps* interpretation methods involve visualizing the gradient (or a related quantity) of the output of a CNN with respect to a given input image (Zeiler and Fergus, 2014; Springenberg et al., 2014; Selvaraju et al., 2017; Sundararajan, Taly and Yan, 2017; Adebayo et al., 2018). We adapted several of these methods for the AJIVE analysis and explored their applicability to our data; unfortunately, none of the methods provided consistently interpretable outputs and raised issues which will be explored in a follow up paper.

Deep learning based predictive analysis of histological images is a growing area (Komura and Ishikawa, 2018; Aeffner et al., 2019; Niazi, Parwani and Gurcan, 2019; Abels et al., 2019) which includes tasks such as classification/regression (Wang et al., 2016; Liu et al., 2017; Bejnordi et al., 2018; Ilse, Tomczak and Welling, 2018; Liu et al., 2018; Veta et al., 2019), semantic segmentation Jiménez and Racoceanu (2019); Mahmood et al. (2019), and microscope augmentation (Chen et al., 2018b) CNN architectures which integrate genetic (or other) information are also being explored for these predictive tasks (Couture et al., 2018; Srivastava et al., 2018; Mahmood et al., 2018). Other studies used non-deep learning based methods to do exploratory, integrative analysis of histological and genetic data Beck et al. (2011); Wang et al. (2013); Cooper et al. (2015)

A similar joint, exploratory analysis of breast cancer H&E image and gene expression data was performed by (Ash et al., 2018). Our methods differ from theirs in a number of ways: they only examined joint signals while we examine both joint and individual signals; they used a sparse CCA while we use AJIVE; we develop and use the RPVs for image interpretation; they trained an auto-encoder while we use transfer learning. An important result of our paper is that even simple transfer learning effectively captures the important signals in the data.

**1.3. Software and data release.** The code to reproduce the analysis in this paper can be found at [github.com/idc9/breast\\_cancer\\_image\\_analysis](https://github.com/idc9/breast_cancer_image_analysis). The raw data e.g. H&E images, gene expression data, clinical variables cannot be released publicly due to patient confidentiality concerns. Researchers may request permission to access the raw data used in this study by visiting <https://unclineberger.org/cbcs/for-researchers/>.

The scikit-image library is used for various image processing tasks (Van der Walt et al., 2014). The PyTorch framework is used for all neural network computations (Paszke et al., 2017). The pre-trained VGG16 weights are downloaded with the PyTorch vision library. We used many of the standard python data science libraries e.g. NumPy Van Der Walt, Colbert and Varoquaux (2011), SciPy Jones, Oliphant and Peterson (2014), sklearn Pedregosa et al. (2011), pandas McKinney (2011), Matplotlib Hunter (2007), and seaborn Waskom et al. (2018). AJIVE computations are done with the py-jive package Carmichael (2019) which was developed for this project.

## 2. Data.

**2.1. CBCS.** The data came from the Carolina Breast Cancer Study, a population-based study of black and white women with invasive breast cancer diagnosed between 2008-2013 in North Carolina. Tumor blocks were collected and cores were transferred from the donor paraffin blocks to prepare tissue microarrays as well as to isolate RNA for gene expression analysis. Tissue preparation and molecular methods are described in (Troester et al., 2017; Allott et al., 2018). The current analysis includes  $n = 1191$  patients for whom both image and gene expression data were available.

For each patient, a pathologist reviewed a paraffin-embedded tumor block and marked the area containing the invasive carcinoma. Then a lab technician extracted a number of circular “cores”, which were then transferred into a recipient TMA paraffin block and eosin (H&E) and imaged. [Supplement A](#) shows a graphical depiction of this process. The upshot is that for each patient we have a median<sup>3</sup> of 4 H&E stained core images. The images of these cores are roughly circular with an average width of approximately 2500 pixels<sup>4</sup>. An example core image is shown in Figure 1. It is appealing to work with cores and not the much larger *whole slide images* because the cores provide more concentrated tumor cells and are more computationally tractable<sup>5</sup>.

Pathologic evaluation of the tumor (including histologic type and grade) was based on the original whole tissue sections. We also compute a number of variables describing image features such as the proportion of white background and the median intensity of the background pixels.

For each patient, we have the PAM50 gene expression measurements, which are 50 genes chosen to distinguish the 5 clinically relevant, genetic subtypes (Basal-like, Luminal A, Luminal B, molecular HER2 and Normal-like) ([Parker et al., 2009](#)). The intrinsic subtype gene list was developed using genes which were consistently expressed within the tumor while minimizing the contribution of the non-tumor microenvironment; therefore the PAM50 genes do not describe the tumor microenvironment ([Perou et al., 2000](#)). We also have a number of variables derived from the PAM50 gene expression such as proliferation score and ROR-PT ([Parker et al., 2009](#)). The ROR-PT is a risk of recurrence score based on both genetic and histological information (e.g. tumor size).

CBCS provides clinically relevant immunohistochemical variables (ER status, clinical HER2 status and PR status), which are derived from routine methods used in the clinical laboratory. Finally, there are other patient variables such as age which are discussed in [Supplement A](#).

The 50 gene expression variables undergo pre-processing which includes centering and scaling by their standard deviation resulting in the gene expression data matrix  $X^{\text{genes}} \in \mathbb{R}^{1,191 \times 50}$ .

**2.2. Image processing and patch representation.** In order to achieve uniform visual stain density, the raw H&E core images are stain normalized using the procedure described in ([Macenko et al., 2009](#)). The set of background pixels of each image (i.e. the whitespace in Figure 1) is then estimated via the following procedure. Each image is converted to grayscale, then a background pixel intensity threshold is estimated with weighted<sup>6</sup> combination of (0.1) Otsu’s method [Otsu \(1979\)](#) and (0.9) the triangle method [Zack, Rogers and Latt \(1977\)](#). The *background mask* (True/False array saying whether or not a pixel is in the background) is then used for a variety of downstream tasks. For example, using the background mask we can estimate the channel wise median background pixel and compute the proportion of background in the entire image.

Next we create a *patch-based* representation of each image. Each core image is broken into a grid of  $200 \times 200$  pixel patches. To make an even grid of patches, the image is first padded with the estimated typical background pixel so its dimensions are divisible by 200. Using the background mask, patches which are more than 90% background are thrown out (Figures 7a and 7b). The background threshold (90%) was selected via manual inspection to be the smallest value such that patches with large amounts of fat and some tissue are still included (Figure 7b).

There are a total of 5,970 core images from the 1,191 subjects resulting in 761,767 patches. We estimate the channel (red, green, blue values for each pixel) mean and standard deviation from the

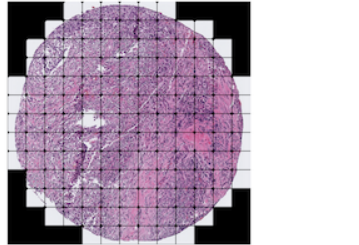
<sup>3</sup>Minimum of 1 and maximum of 8.

<sup>4</sup>Min 600, max 3400.

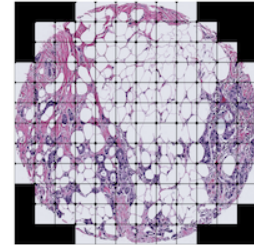
<sup>5</sup>The whole slide images can be of order  $50,000 \times 50,000$  pixels or larger.

<sup>6</sup>Through exploratory analysis we noticed that off the shelf methods (e.g. Otsu alone) had systemic issues with images which have a high proportion of background (e.g. those with a high fat content or high mucin content). This particular combination was selected by tuning on a visual examination of the 100 images with the highest proportion background.

patch dataset. Before being input into the neural network, each pixel channel is mean centered then scaled by the standard deviation.



(a) The patch grid for an example core.



(b) A core with high fat content.

Fig 7: Patch grid for two example cores, one with low fat content (a) and one with high fat content (b). Black squares indicate patches with too much background that were excluded. The background threshold is selected such that the thin pieces of tissue surrounding fat cells (and other structures with lots of white space such as mucin) are included.

**2.3. CNN feature extraction.** After the raw images are processed, CNN features are extracted from each patch. We use the last convolutional layer of the VGG16 architecture [Simonyan and Zisserman \(2014\)](#) with an additional *spatial mean pooling* layer added to the end of this architecture to average out spatial information resulting in 512 CNN features. In other words, if the output from the original network applied to a  $200 \times 200 \times 3$  pixel image is sized  $H \times W \times 512$  (where 512 is the depth), the spatial mean pool will output a 512 dimensional vector. The pre-trained weights of the network are downloaded from the torch vision library. No additional fine-tuning is performed (see Section 5.0.2 for discussion).

Finally, core-images are represented as an average of their patch features (again, ignoring patches which are over 90% background). Patients are then represented by an average of their cores. [Supplement A](#) provides a graphical representation of this process. Each CNN feature is first mean centered then scaled by its standard deviation resulting in the image feature data matrix  $X^{\text{image}} \in \mathbb{R}^{1,191 \times 512}$ .

**3. Methods.** A key challenge for doing statistical inference on populations of images with deep learning is interpretability. In section 3.1 we explain the novel, broadly applicable RPV method for interpretation of the visual signals captured by neural network features. In Section 3.2 we give an overview of the AJIVE procedure. Section 3.3 describes the pathology review process for interpreting the AJIVE image modes of variation.

**3.1. Representative patch views.** The RPV assumes that images<sup>7</sup> are represented via the patch based approach described in Sections 2.2 and 2.3. In other words, images are broken into a collection of patches; CNN features are extracted for each patch then images are represented as an average of their patch features. Suppose we compute a loadings vector of image features (e.g. the first image PCA component). The RPV illustrates one end of a loadings vector (e.g. the positive end of PC 1). For each end of one component, we select the top 15 subjects (e.g. the subjects with the 15 most positive PC scores) then create the RPVs for each of these subjects.

Figure 8 shows an example RPV displaying one subject for the negative end of AJIVE joint component 1. The leftmost column shows the four cores for this subject. The rightmost five columns

<sup>7</sup>In the CBGS study each subject has a number of core-images and subjects are represented as an average of their images. For exposition purposes we pretend each subject has one image in this section, however, the extension to the multi-image case is clear.

show the top 20 patches for the negative end of the first joint component from the *patch based localization* approach described below in Section 3.1.1. The second column shows the location on each core of the top 20 patches. The RPVs are multi-scale in the sense that they give insights at both the core level and the patch level.

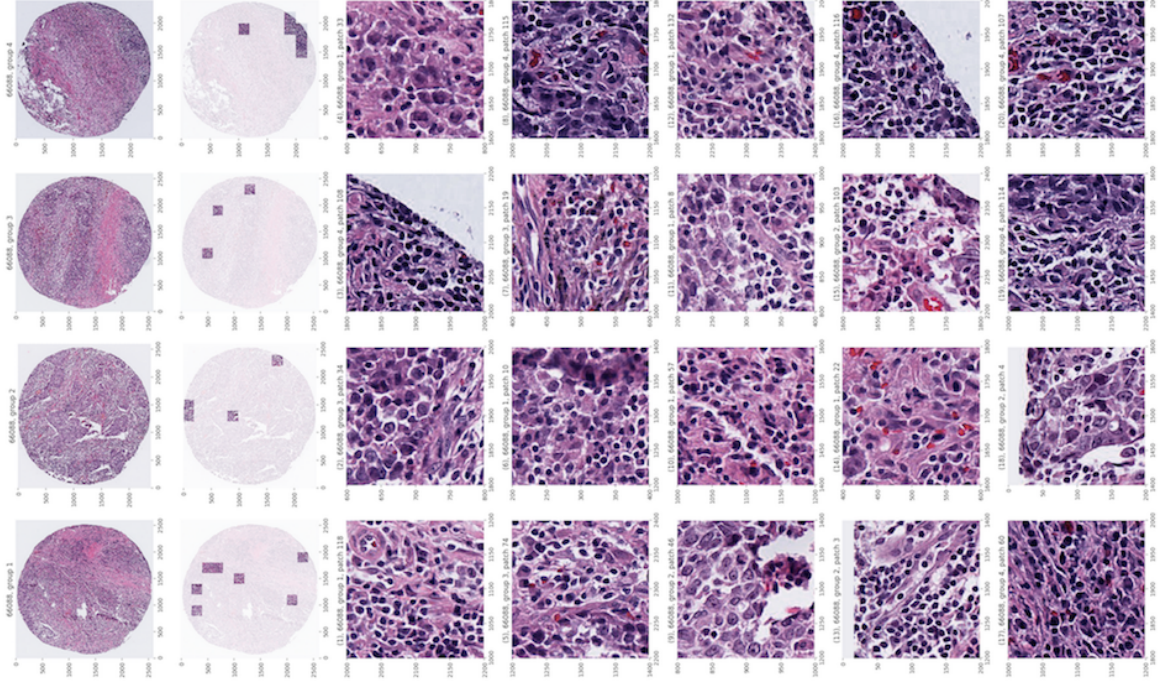


Fig 8: The full representative patch view from Figure 3. The first column shows the 4 cores for this subject (high resolution is needed to see detail). The 20 patches (Section 3.1.1) in the last 5 columns are representative of the visual features associated with one extreme of a mode of variation. The second column shows the patches' locations on the cores. Lymphocytes show up prominently in these patches. Some images (1, 8, 11, 18) show predominantly tumor cells, and others (10, 14, 15) show a roughly even mixture of lymphocytes and tumor cells.

**3.1.1. Patch based localization.** Here we describe the general approach used to select the representative patches for the RPVs described in the above section. Patch based localization is accomplished by projecting patches onto the loadings vector. Main ideas are illustrated below in the context of PCA but this approach is quite general.

Let  $n$  be the number of subjects (images) in the dataset,  $m_i$  be the number of patches for the  $i$ th image,  $p_{ij}$  be the  $j$ th patch for the  $i$ th subject,  $f : \text{image} \rightarrow \mathbb{R}^k$  the feature extraction network outputting  $k$  features. Also let  $z_{ij} := f(p_{ij})$  be the features for patch  $p_{ij}$ ,  $z_i := \frac{1}{m_i} \sum_{j=1}^{m_i} z_{ij}$  be the average patch features for the  $i$ th subject,  $Z \in \mathbb{R}^{n \times k}$  be the image feature dataset, and  $\tilde{Z} \in \mathbb{R}^{n \times k}$  be  $Z$  after processing (e.g. centering and scaling). Let  $\mathbf{v} \in \mathbb{R}^k$  be a loadings vector and  $\mathbf{u} = \tilde{Z}\mathbf{v} \in \mathbb{R}^n$  the scores vector<sup>8</sup> computed from  $\tilde{Z}$  (e.g. PC component 1).

Consider the positive end of this component and let  $i^*$  be the index of a particular image. We perform *patch based localization*<sup>9</sup> by projecting every patch of subject  $i^*$  onto  $\mathbf{v}$ . In detail, let  $\tilde{z}_{i^*,j}$

<sup>8</sup>We assume that the scores are the projection of the data onto the loadings vector.

<sup>9</sup>We use the term localization because this method helps identify which regions in the image are playing an important role in the given mode of variation.

be the features of the  $j$ th patch for subject  $i^*$  after the processing. Let  $s_{i^*,j} := \tilde{z}_{i^*,j}^T \mathbf{v}$  be the scores of this patch for  $j = 1, \dots, m_{i^*}$ . Now let  $j_{(1)}, \dots, j_{(20)}$  be the indices of the patches with the 20 most positive patch scores (i.e.  $s_{i^*,j_{(1)}} \geq s_{i^*,j_{(2)}} \dots$ ). We call these the *representative patches* for the positive end of this component.

Principal components analysis can be viewed as finding important modes of variation in the data. If we used “interpretable” features, then inspecting the top entries of the loadings vector,  $\mathbf{v}$ , would shed light on what this given mode of variation is about. Unfortunately, for uninterpretable features such as abstract neural features, inspection of a loadings vector does not provide much interpretable information. Note this visualization procedure can be applied to statistical algorithms other than PCA; it simply requires an algorithm that outputs loadings vectors of neural features.

**3.2. Angle-based joint and individual variation explained.** *Angle based joint and individual variation explained* (AJIVE) is a statistical feature extraction/dimensionality reduction algorithm for multi-block data (Feng et al., 2018). The goal of AJIVE is to find joint signals, if any exist, which are common to all data blocks as well as individual signals which are specific to each block, if they exist. Here we give a brief overview of AJIVE for two data blocks.

Consider two data blocks  $X \in \mathbb{R}^{n \times d_x}$ ,  $Y \in \mathbb{R}^{n \times d_y}$  on the same set of  $n$  observations. AJIVE estimates what variation is *joint* to both data blocks as well as what variation is *individual* to each block. In particular, each matrix is decomposed into a sum of *joint*, *individual*, and *error* terms,

$$X = J^x + I^x + E^x \text{ and } Y = J^y + I^y + E^y$$

while imposing the following constraints

- $\text{col-span}(J^x) = \text{col-span}(J^y) := \mathcal{J} \subseteq \mathbb{R}^n$
- $\text{col-span}(J^x) \perp \text{col-span}(I^x)$  and  $\text{col-span}(J^y) \perp \text{col-span}(I^y)$
- $\text{col-span}(I^x) \cap \text{col-span}(I^y) = \emptyset$

All subspaces live in  $\mathbb{R}^n$  where  $n$  is the number of observations. The two joint matrices span the same *joint subspace*,  $\mathcal{J}$ . The two individual matrices span subspaces which are orthogonal to the joint subspace. We refer to the rank of the joint subspace as the *joint rank*,  $R_J$ , and the rank of the two individual subspaces as the  $X$  and  $Y$  individual ranks,  $R_x, R_y$ .

The mechanics of AJIVE are outlined below for the case of  $B = 2$  data blocks<sup>10</sup>. The properties of the common normalized scores discussed below follow from the fact they are the subspace flag mean of the PCA scores subspaces Draper et al. (2014). We use a different estimate of the block common loadings,  $L^x, L^y$  than in the original paper. One of the key statistical procedures in AJIVE is to estimate the joint rank<sup>11</sup> which is achieved using the Wedin bound and the random direction bound detailed in (Feng et al., 2018).

1. **Initial signal extraction:** Estimate low rank PCAs of  $X, Y$  with ranks  $r_{\text{init}}^x, r_{\text{init}}^y$  (e.g. selected by inspecting the PCA scree plots). Denote this initial PCA of  $X$  by  $U_{\text{init}}^x, D_{\text{init}}^x, V_{\text{init}}^x$  where  $U_{\text{init}}^x \in \mathbb{R}^{n \times r_{\text{init}}^x}$ ,  $V_{\text{init}}^x \in \mathbb{R}^{d_x \times r_{\text{init}}^x}$ . Similarly for  $y$ .
2. **Signal space extraction:** Perform CCA on the PCA scores,  $U_{\text{init}}^x, U_{\text{init}}^y$ . Using the *random direction bound* and the *Wedin bound* estimate the CCA rank,  $R_J$ . Let  $S^x, S^y \in \mathbb{R}^{n \times R_J}$  be the matrices whose columns are the x/y CCA scores with unit norm. Let  $W^x \in \mathbb{R}^{r_{\text{init}}^x \times R_J}, W^y \in \mathbb{R}^{r_{\text{init}}^y \times R_J}$  be the matrices whose columns are the CCA x/y loadings. Let  $C \in \mathbb{R}^{n \times R_J}$  be the *common normalized scores* which have the property of being proportional to the average of

<sup>10</sup>The original paper describes the procedure some what differently, but this description is equivalent.

<sup>11</sup>This is accomplished by estimating which principal angles between  $\text{col-span}(U_{\text{init}}^x)$  and  $\text{col-span}(U_{\text{init}}^y)$  are smaller than random in an appropriate sense.

the  $x/y$  CCA scores. In other words, the  $j$ th column of  $C$  is unit norm and is proportional to the average of the  $j$ th columns of  $S^x$  and  $S^y$ . Additionally the common normalized scores are orthonormal i.e.  $C^T C = I_{R_J}$ . Finally, let<sup>12</sup>  $L^x := V_{\text{init}}^x D_{\text{init}}^{x^{-1}} W^x \in \mathbb{R}^{d_x \times R_J}$  be the  $x$ -*common loadings*. Similarly for  $y$ .

3. **Signal space extraction:** Let  $J^x := C C^T X$  be the estimated joint matrix. Let  $\tilde{I}^x := (I - C C^T) X \in \mathbb{R}^{n \times d_x}$ . Let  $R_x$  be the number of singular values of  $\tilde{I}^x$  above the threshold discussed in Section 2.4 of [Feng et al. \(2018\)](#) and let  $I^x \in \mathbb{R}^{n \times d_x}$  be the rank  $R_x$  SVD approximation of  $\tilde{I}^x$ . We denote the PCA of the individual matrix  $I^x$  by  $U_{\text{individual}}^x \in \mathbb{R}^{n \times R_x}$ ,  $D_{\text{individual}}^x \in \mathbb{R}^{R_x \times R_x}$ ,  $V_{\text{individual}}^x \in \mathbb{R}^{d_x \times R_x}$  which is also of interest. Similarly for  $y$ .

The outputs of interest in this paper are the following

- The joint rank,  $R_J$ .
- The *common normalized scores*,  $C \in \mathbb{R}^{n \times R_J}$ .
- The *common loadings*<sup>13</sup>,  $L^x \in \mathbb{R}^{d_x \times R_J}$ ,  $L^y \in \mathbb{R}^{d_y \times R_J}$ .
- The  $U_{\text{individual}}^x \in \mathbb{R}^{n \times R_x}$  and  $V_{\text{individual}}^x \in \mathbb{R}^{d_x \times R_x}$ , which are referred to as the *block specific, individual scores and loadings*. Similarly for  $y$ .

The common loadings,  $L^x, L^y$  are different than those in [\(Feng et al., 2018\)](#). The loadings computed here are the loadings such that  $XL^x + YL^y \propto C$  i.e. the average of the resulting scores are proportional to the common normalized scores. Computing the loadings in this way ensures that they incorporate joint information only.

**REMARK 3.1.** *It can be checked that the random direction bound is equivalent to the classical Roy's largest root test CCA rank selection method ([Johnstone, 2008](#)).*

3.2.1. *AJIVE analysis of CBCS data.* The only variables used in the AJIVE analysis are the 512 CNN image features and expressions for 50 genes from PAM50; the other variables are used to interpret the AJIVE results. The initial signal ranks are 81 (image features) and 30 (genes) and were selected by inspection of the difference of the log-singular values and airing on the side of picking too high a rank. AJIVE estimates a joint rank of 7, image individual rank of 76 and genetic individual rank of 25. The AJIVE diagnostic plot, detailed in [Feng et al. \(2018\)](#), is provided in [A.2](#).

3.3. *Pathology review of images.* In close collaboration with pathologists (B.C. and J.G.), we reviewed the first three joint and image individual components at two levels of granularity. Tables [1](#) and [3](#) summarize the pathologists' observations of these components. These observations are key to understanding the connections between the pathology and the genetics.

In the first approach, which we refer to as *global sort*, all core images are reviewed in sequence after sorting by the patient scores. Joint components are sorted by common normalized scores,  $C$ , and individual components are sorted by block specific scores,  $U_{\text{individual}}^{\text{image}}$  (see Section [3.2](#)). After sorting, the images are reviewed in sequence (e.g. from the negative to the positive end) to explore the visual signals captured by a given component. The benefits of the global sort method are i) a large number of images are inspected ii) we get a sense of the high level changes<sup>14</sup> as we move along a component from the extreme negative to the middle then to the extreme positive end and

<sup>12</sup>Note the  $j$ th column of  $V^x$  is equivalent to the rank  $r_{\text{init}}^x$  principal components regression coefficient of the  $j$ th column of the common normalized scores,  $C$ , regressed on the  $X$  matrix.

<sup>13</sup>These were not given names in the [Feng et al. \(2018\)](#) and were computed slightly differently.

<sup>14</sup>In a preliminary analysis where image patches with a large amount of background were not excluded (see Section [2.2](#)), the global sort method on the first few principal components revealed that the primary modes of variation in the data are driven by the raw amount of background. This motivated the exclusion of patches with too much background.

iii) we can see if the trends found in the RPVs (see next paragraph) hold broadly for the entire component. The downsides of this method are that it is time intensive and does not provide explicit information about what visual signals are important in a given image. The H&E images are quite large and complex and finding patterns across a set of images is challenging.

The RPV approach developed in Section 3.1 extracts more fine-grained information at the patient level. The RPVs of the 15 most negative and 15 most positive subjects are inspected for each component. The RPVs are created with the common loadings  $L^{\text{image}}$  for the joint components and the block specific individual loadings  $V_{\text{individual}}^{\text{image}}$  (see Section 3.2). The number 15 was selected to balance showing “enough” information without taking too much time. The RPVs have the benefit of highlighting a more focused set of visual patterns.

Tables 1 and 3 display the pathologist’s observations based on the RPVs at each end of each component. Each column summarizes the pathologist’s impression of a clinically relevant histological feature. The *homogeneous* column indicates whether or not there appeared to be a consistent pattern across the reviewed RPVs. The global sort review shows these trends hold for more than just the 15 most extreme images.

**4. Results.** This section discusses the results for the joint AJIVE components (Section 4.1), the image individual (Section 4.2) and genetic individual (Section 4.3). For the sake of time – both the readers’ and the pathologists’ – we focus on the top 3 components from each of the joint, image individual and genetic individual.

The pathology review of the images from the joint and image individual components is described in Section 3.3. While the pathologist reviewed the full RPVs (Figure 8), only mini-RPVs (e.g. Figure 9a) displaying 8 patches are shown below. The full RPVs shown to the pathologists, all AJIVE genetic loadings, and all clinical data comparisons are provided in [Supplement A](#). The methodology for clinical data comparisons (e.g. multiple testing control) is discussed in Section A.3.

**4.1. Joint image and genetic information.** Table 1 summarizes the pathologist’s observations based on the RPVs of the first three joint components. Component 1 was discussed in Section 1.1.

component	end	homogeneous	tumor cellularity	tubule formation	nuclear grade	adipocytic stroma	collagenous stroma	lymphocytes	necrosis
1	positive	no	low	yes	1, 2	yes	yes	no	no
	negative	yes	high	no	3	no	limited	yes	yes
2	positive	no	variable	yes	3	focal	yes	few	no
	negative	yes	moderate/high	yes	2	focal	yes	no	no
3	positive	no	variable	yes	3	yes	limited	yes	no
	negative	yes	moderate/high	no	3	no	yes	no	no

TABLE 1

*A pathologist’s summary of important clinical features based on the RPVs of the 15 most extreme subjects for each end of the first three joint components. The “homogeneous” column indicates whether or not the patterns shown in the RPVs were consistent across the 15 subjects.*

Component	ER status	Clinical HER2 status
1	0.883 (+)	0.558
2	0.752 (-)	0.617 (+)
3	0.551	0.777 (-)

TABLE 2

*AUC scores for two immunohistochemical (IHC) variables, ER status and clinical HER2 status (positive vs. negative classes), for first three joint components based on AJIVE common normalized scores. All six of these comparisons are statistically significant. The sign in parentheses indicates which end of the component the IHC positive status cluster on if there was a clear visual separation in the histogram (see [Supplement A](#)). For example, ER status positive tumors cluster on the positive end of component 1.*

4.1.1. *Joint component 2*. From the pathology perspective, the tumors on the negative end of joint component 2 show mostly collagenous stroma surrounded by moderate nuclear grade tumor cells. Figure 9 shows the mini-RPVs of two subjects from the negative end of the second joint component. The positive end of this component was not homogeneous (Table 1).

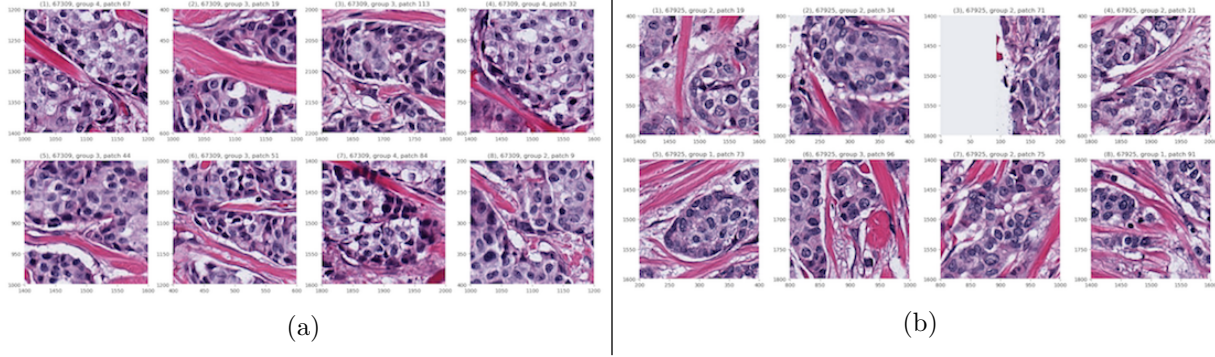
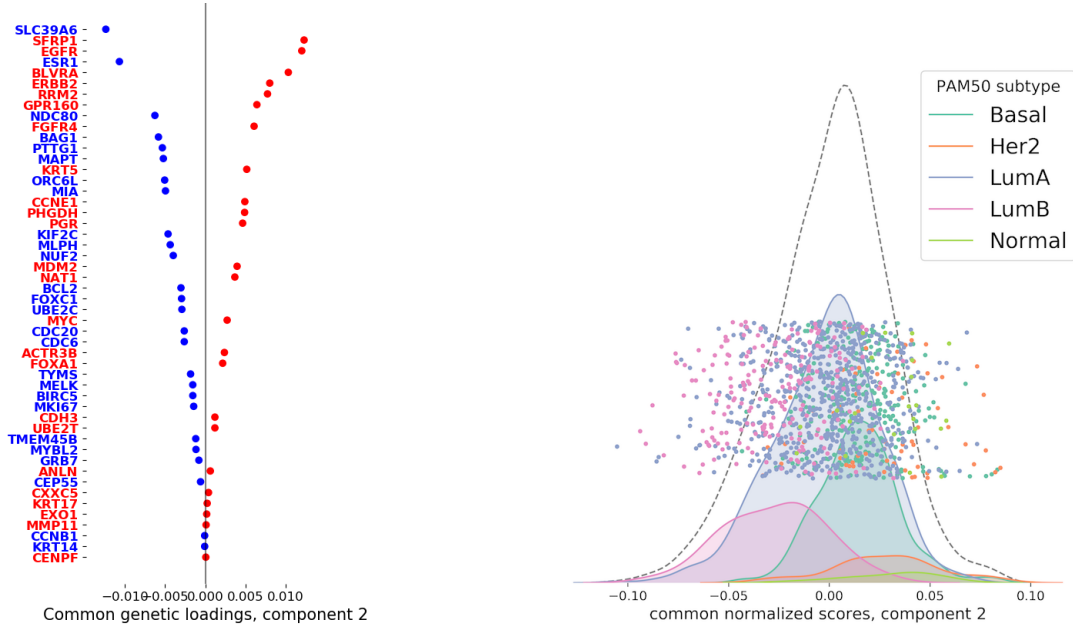


Fig 9: Two tumors from the negative end of joint component 2. Both RPVs show collagenous stroma (light pink, stringy tissue) surrounded by moderate nuclear grade tumor cells and moderate tumor cellularity. The tumor in (a) is genetically Luminal B and the tumor in (b) is Luminal A.



(a) Joint component 2, PAM50 loadings. (b) Joint component 2 scores conditioned on PAM50 subtype.

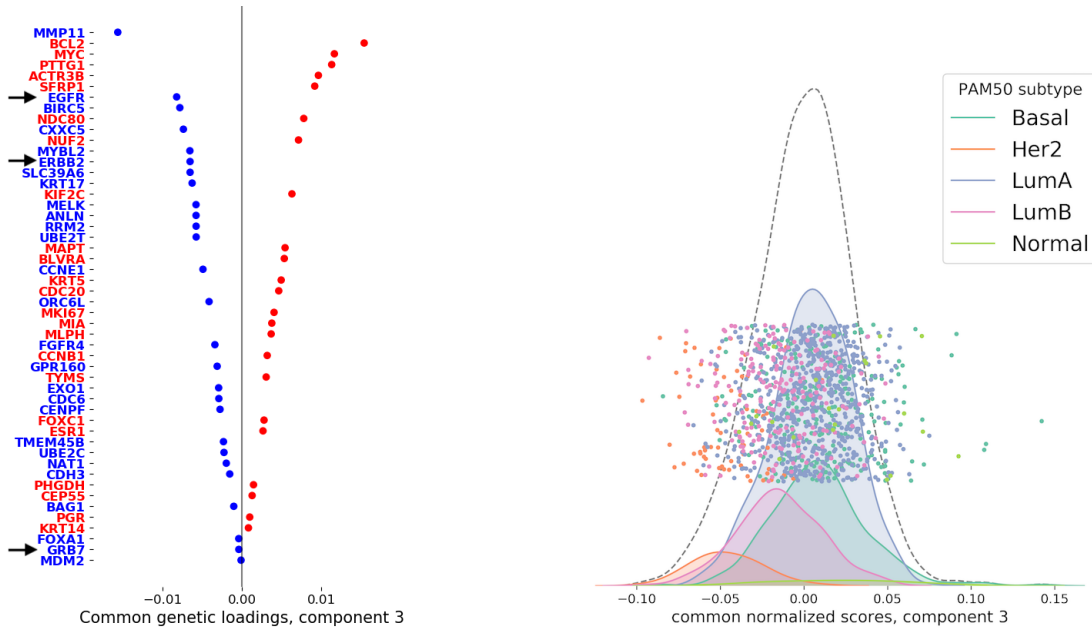
Fig 10: The Luminal B and Luminal A classes are associated with the negative end of joint component 2. Not much is known about this histology of Luminal cancers.

From the genetics perspective, the negative end of joint component 2 picks out the Luminal B subtype (Figure 10b). Looking at the PAM50 loadings vector, ESR1, SLC39A6 are the two most negative genes in the PAM50 loadings (Figure 10a) and are known to be high in clinically ER+ cancers (Parker et al., 2009). The Luminal B observations cluster on the negative end of

this direction and are statistically significantly separated from the other PAM50 subtypes with AUC scores of: Basal = 0.905, HER2 = 0.933, Luminal A = 0.760, Normal = 0.950 (Figure 10b).

From the immunohistochemical perspective, the second joint component is moderately related to ER status while weakly related to clinical HER2 status (Table 2). Clinical ER positive tumors cluster on the negative end of this component with an AUC of 0.752.

The pathology perspective of this second joint component appears to pick up on morphological features of Luminal B tumors i.e. intratumoral channels of stromal cells which are surrounded by moderate nuclear grade cancer cells. To our knowledge, little is known about the histological features of Luminal B tumors. Interestingly, Beck et al. (2011) used image analysis approaches to demonstrate connections between certain stroma morphological features and patient survival. Pathologists do not currently use stromal features in the diagnosis and classification of tumors. However, tumor stroma and microenvironment (Eiro et al., 2019) and the stromal features of benign and tumor-adjacent normal tissue (Román-Pérez et al., 2012; Chollet-Hinton et al., 2018) are areas of active investigation. Recent studies using CNNs have shown that breast biopsies may be accurately classified as malignant solely based on stromal features (Bejnordi et al., 2018).



(a) Joint component 3, PAM50 loadings. (b) Joint component 3 scores conditioned on PAM50 subtype.

Fig 11: The molecular HER2 subtype are associated with the negative end of joint component 3.

**4.1.2. Joint component 3.** From the genetics perspective, the negative end of joint component 3 picks out molecular HER2. The HER2 observations are separated from the other PAM50 subtypes with AUC scores of: Basal = 0.947, Luminal A = 0.940, Luminal B = 0.833, Normal = 0.950. Interestingly, ERBB2 and EGFR have large negative values in the joint loadings vector while GRB7, which is on the same *amplicon* as ERBB2, is almost 0 (Figure 11a). The negative end of this component is also moderately related to clinical HER2 status with an AUC of 0.777 (Table 2). This component is identifying not only clinical HER2 samples (as determined by IHC staining) but more strongly the molecular HER2 subtype of samples (as determined by gene expression). Previous work (Network et al., 2012) has shown both gene expression and protein and phosphoprotein levels of

ERBB2 and EGFR are significantly enriched in clinically HER2 samples that are also the molecular HER2 subtype compared to clinical HER2 samples that are Luminal subtypes. This is consistent with the separations we see in joint component 3.

From the pathology perspective, the negative end joint component 3 again shows collagenous stroma, but this time surrounded by high nuclear grade tumor cells (Figure 12). Recall joint component 2 was similar but with moderate grade tumor cells. This third joint component appears to be picking up on morphological features of molecular HER2 tumors. Similar to joint component 2, it is interesting that the stroma appear to play an important role in this component.

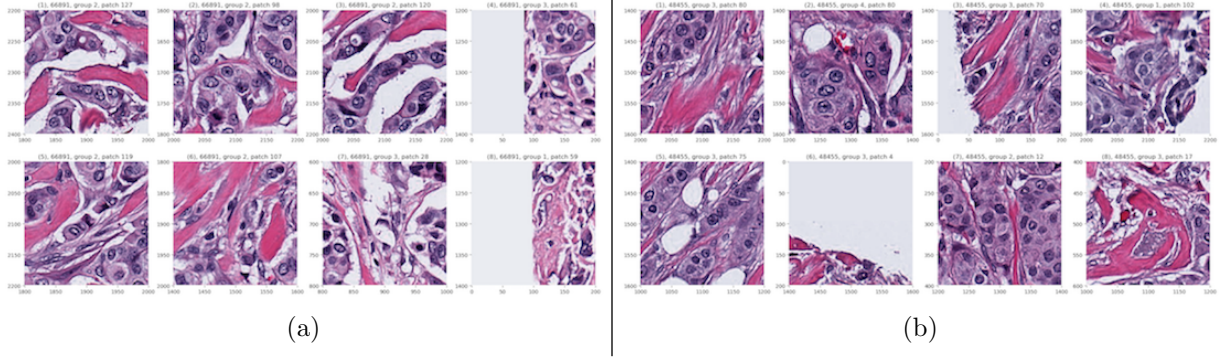


Fig 12: Tumors from the negative end of joint component 3 showing tumor cells surrounded collagenous stroma.

**4.2. Image individual information.** As mentioned in Section 2.1, the PAM50 genes were selected to emphasize genes expressed in tumor epithelium, not genes highly expressed in tumor microenvironment features such as fat cells, collagenous stroma, and in some cases mucin. Several of these microenvironment features have clear visual signals (e.g. high fat content images have round, clear adipose cells) and show up prominently in the AJIVE individual components.

component	end	homogeneous	tumor cellularity	tubule formation	nuclear grade	adipocytic stroma	collagenous stroma	lymphocytes	necrosis
1	positive	yes	low	focal	1, 2	yes	limited	few	no
	negative	yes	variable	no	2	no	yes	few	some
2	positive	yes	moderate	no	2, 3	focal	yes	yes	no
	negative	yes	low	no	1	focal	limited	no	no
3	positive	yes	low	yes	2	focal	yes	few	no
	negative	yes	low	no	2	yes	no	no	no

TABLE 3

*A pathologist's observations of first three image individual components from RPVs of 15 most extreme subjects on either end of the component.*

**4.2.1. Image individual component 1.** All of the images on the positive end of the first image individual component shows a very clear theme of tumors with high fat content (Figure 13). High fat content is a strong visual signal so it makes sense that it shows up as an early individual mode of variation for image data. The negative end of the first image individual component shows tumors with low tumor cellularity and low/moderate grade nuclei (Table 3 and Figure 14).

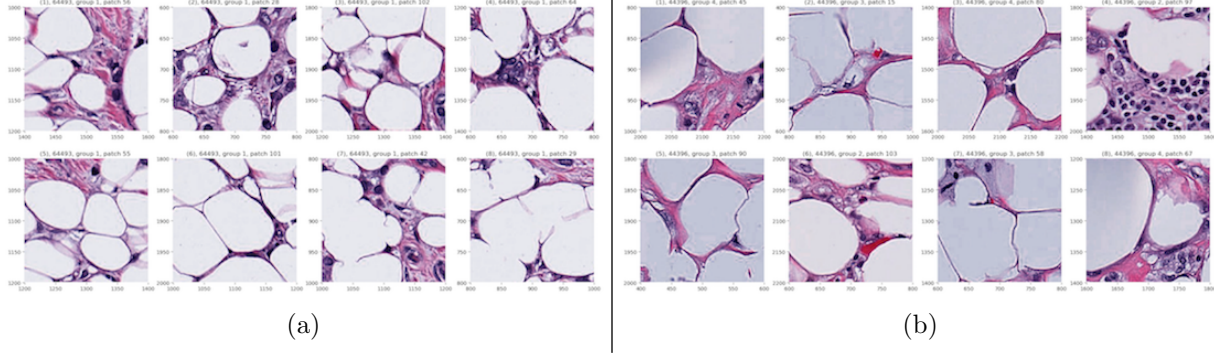


Fig 13: Two tumors from the positive end of image individual component 1 showing high fat content.

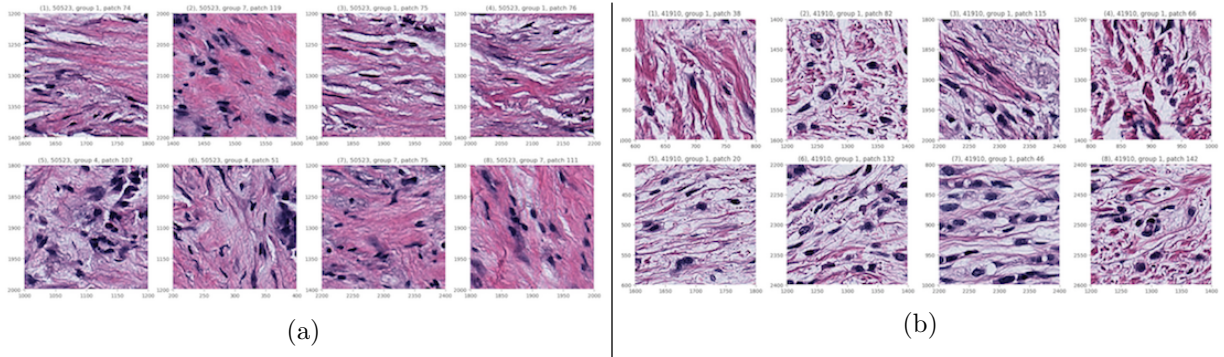


Fig 14: Two tumors from the negative end of image individual component 1 showing moderate nuclear grade, variable tumor cellularity, collagenous stroma.

**4.2.2. Image individual component 2.** The negative end of image individual component 2 clearly picks out *mucinous carcinoma* tumors (Figure 15). Mucinous carcinomas are characterized by tumor cells floating in pools of mucin. These cancers presents a very clear visual pattern of dark purple tumor cells surrounded by wispy looking mucin. Mucinous carcinoma is a rare histological subtype which the PAM50 genes [Perou et al. \(2000\)](#) are not designed to identify.

Mucinous carcinomas are typically low-grade, hormone receptor-positive, have a good prognosis and appear to be genetically different from invasive ductal carcinomas of no special type ([Diab et al., 1999](#); [Di Saverio, Gutierrez and Avisar, 2008](#); [Weigelt et al., 2009](#); [Lacroix-Triki et al., 2010](#)). Mucinous carcinomas are usually genetically Luminal-type (typically Luminal A) ([Colleoni et al., 2011](#); [Caldarella et al., 2013](#); [Weigelt et al., 2009](#)). All of the top 15 tumors on the negative end of this component are genetically Luminal (12 are Luminal A and 3 are Luminal B). Interestingly, neither the Luminal A nor B classes are strongly associated with the individual scores for this component overall; none of the difference in distribution tests (Section A.3) for Luminal A vs. another class were statistically significant (similarly for Luminal B). This is consistent with variation appearing in an image individual component.

The positive end of individual component 2 picks out images with moderate cellularity and collagenous stroma surrounded by moderate nuclear grade tumor cells.

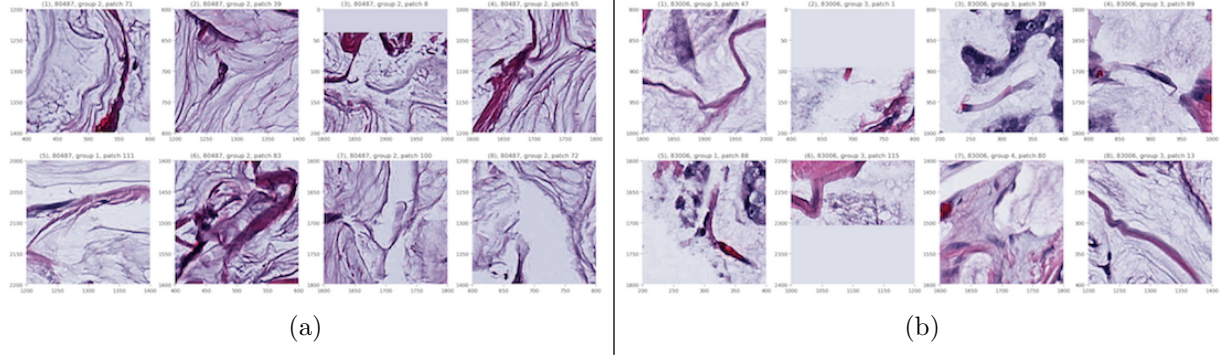


Fig 15: Two tumors from the negative end of image individual component 2 both displaying mucinous carcinomas.

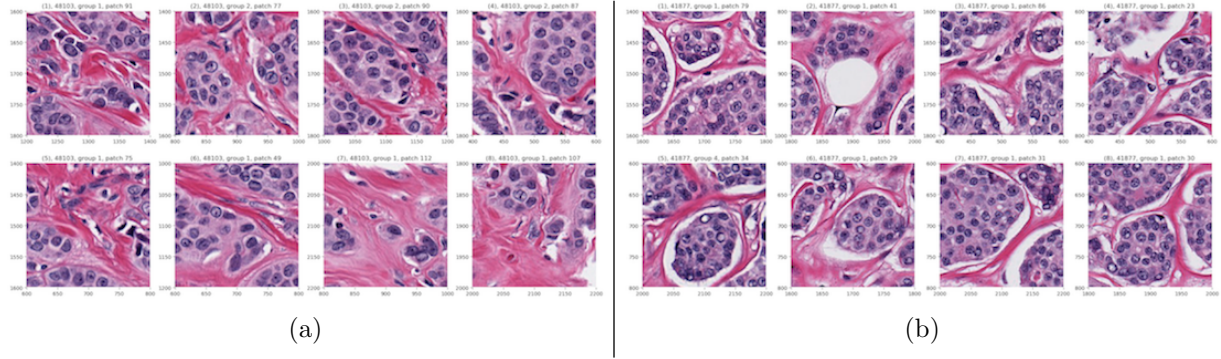


Fig 16: Two tumors from the positive end of image individual component 2 both showing: collagenous stroma, moderate to high nuclear grade, moderate tumor cellularity.

The positive and negative ends of image individual component 2 show contrasting histologic features. The patches from the tumors on the positive end are entirely filled with a combination of tumor cell aggregates separated by areas of dense collagenous stroma. Adipocytic stroma is absent and the only optically clear space is in areas of retraction artifact where tumor cell groups appear to be pulled away from adjacent stroma (a known artifact of histologic preparation in some invasive tumors). The patches from the negative end show extracellular mucin from mucinous carcinomas with low or no tumor cellularity and just a few wispy bands of stromal collagen. The contrasting histology raises the possibility that this component may separate tumors based on one or more of the following features: tumor cellularity, tumor grade, extracellular stromal composition.

**4.2.3. Image individual component 3.** The negative end of image individual component 3 picks up on tumors whose patches contain a large amount of optically clear space. This includes tumors with: with high fat content (Figure 17b), where the cells discohesive (Figure 17c) and disrupted tissue sections (Figure 17a). Recall (Section 2.2) that patches with too much background (over 90%) are removed. Therefore white space surrounding the tumors and large white spaces in the core are unlikely to influence the amount of white space in the patches representing the image. Some of the features seen in the images in Figure 17 17a and 17c are likely related to technical variation in the tumor fixation/preservation and the quality of the histologic preparation. While the high fat content pattern seen in the positive end of the first image individual component is similar

to this component (i.e. it picks up on large amounts of white space) the first component uniformly contains high fat content images in the top 15 images which is unlike this third component.

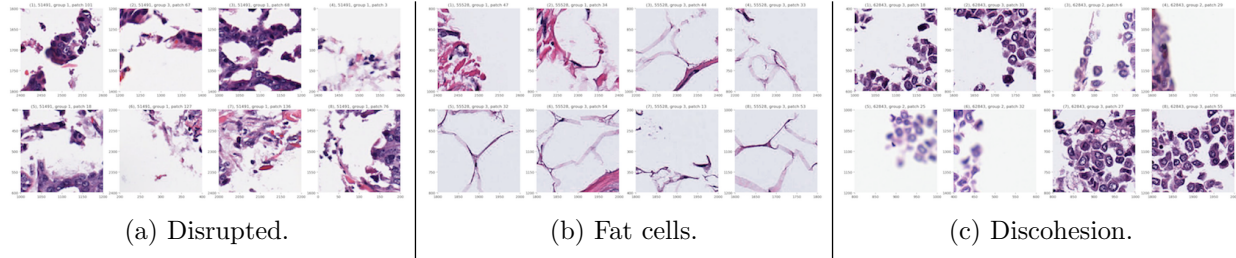


Fig 17: Three tumors from the negative end of image individual component 3 all showing the clear visual pattern of a large amount of optically clear space.

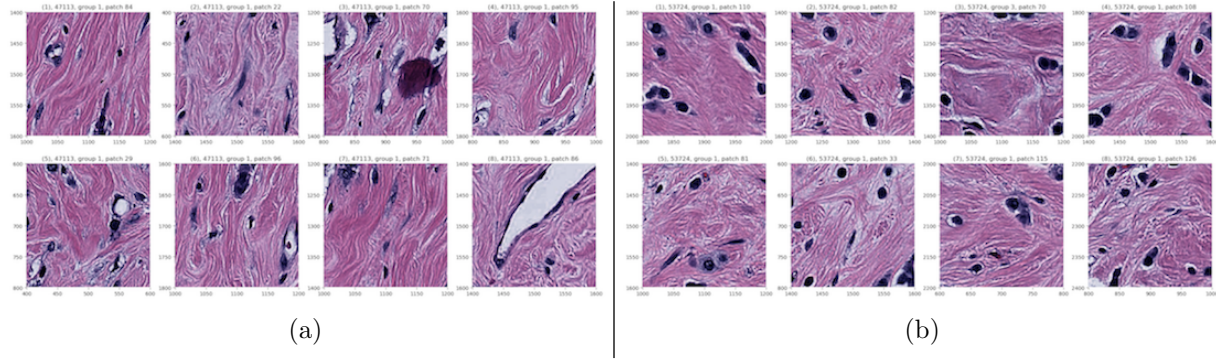


Fig 18: Two tumors from the positive end of image individual component 3. Both show a visually clear pattern of dense collagenous stroma, low tumor cellularity, moderate nuclear grade, some lymphocytes.

The positive end of this third component picks on images with a large amount of dense collagenous stroma (Figure 18). This pattern is very clear in all 15 of the most positive subjects' representative images views (see [Supplement A](#)). These tumors have lower tumor cellularity, moderate nuclear grade and have a moderate number of lymphocytes. Similar to the amount of white space, the dense collagenous stroma is a clear visual pattern.

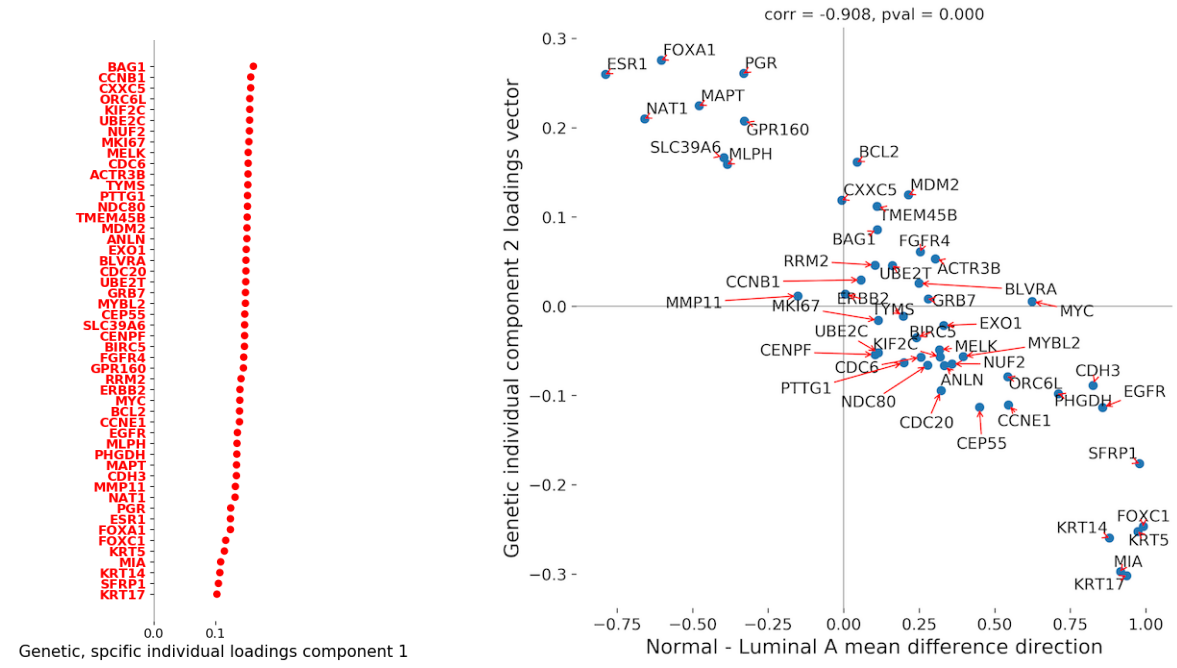
**4.3. Genetic individual information.** Figure 19a shows the PAM50 loadings vector of the first genetic individual component. This component picks up on overall gene expression levels which is a common source of technical variation. Both the second and third genetic individual components show connections to the PAM50 subtypes based on the clinical data comparisons given in [Supplement A](#) albeit with weaker separations than the joint components.

The second genetic individual component identifies additional information which varies between Luminal A and Normal that is not dependent on cell proliferation and seems to be more related to features such as estrogen receptor signaling and keratin expression status. The scores for this second component separate Normal-like from Luminal A with an AUC of 0.801.

Figure 19b shows a scatter plot of the loadings vector from genetic individual component 2 compared to the Normal-Luminal A mean difference direction<sup>15</sup>. Several of the genes on the top

<sup>15</sup>The genes were first scaled by their standard deviation so this is the naive Bayes classification direction.

left of 19b (ESR1, FOXA1, PGR) are all part of the estrogen signaling pathway (Oh et al., 2006). Several of the genes in the middle (CCNB1, MYC, MKI67, TYMS, MYBL2, CCNE1) are related to proliferation suggesting this component is unrelated to proliferation. Several of the genes in the bottom right (KRT5, KRT14, KRT17) are characteristic of normal myoepithelium as well as Basal-like like breast cancer (Lazard et al., 1993).



(a) Genetic individual component 1 loadings shows common genetic technical mode of variation not expected to be associated with the images.

(b) Genetic individual component 2 loadings vector compared to Normal-Luminal A mean difference direction. Luminal A is on the left (negative) while Normal-like is on the right (positive).

Fig 19: Genetic individual components show technical variation as well as additional PAM50 subtype information.

**5. Conclusion.** This paper develops methods that, using deep learning and AJIVE give interpretable, simultaneous image and genetic results. Inferential and exploratory analysis leveraging deep learning is a promising area which presents many interesting, open questions – some of which are discussed below. These analytical tools enable simultaneous engagement from both the pathology and genetic communities which is critical for the fundamental biomedical interpretations.

Future research should evaluate whether the features learned in this paper can be reproducibly identified by pathologists and/or automated computer vision systems as well as whether these features can be validated in external test sets.

Scaling histological image analysis pipelines to gigapixel *whole slide images* (WSI) is an important future direction. In clinical practice, pathologists use WSIs; the core images used in this paper require additional preparation, are typically only available in some research settings and may ignore important tumor information (e.g. spatial heterogeneity across the tumor, particularly histological patterns not observed in the sampled region). Analyses of WSIs presents computational challenges as these images are orders of magnitude larger than the core images.

5.0.1. *Patch representation.* Patch based approaches have shown promise for predictive tasks using deep learning Ilse, Tomczak and Welling (2018). The patch based approach taken in this paper was selected because it i) will scale to whole slide images ii) can identify localized image information e.g. with the RPVs and iii) creates a smaller feature set<sup>16</sup>. The approach of averaging of patch features ignores some within image heterogeneity. For image-only analysis, methods such as Bishop and Tipping (1998); Backenroth et al. (2018) may be able to capture additional within-image heterogeneity. In the context of multi-view data, additional methodology needs to be developed to account for grouped observations (e.g. Pourzanjani et al. (2017)).

5.0.2. *Transfer learning.* Training a neural network can be time and resource intensive. Furthermore, CNNs often require a large amount of training data to be fit effectively. Transfer learning allows the data analyst to use more powerful neural networks with less data and less time spent tuning CNN parameters (Yosinski et al., 2014; Sharif Razavian et al., 2014). First, a CNN is trained to solve a different predictive task on a large, external dataset – typically the famous ImageNet classification task (Deng et al., 2009). Then the pre-trained network parameters may be *fine-tuned* on the dataset of interest to solve the predictive problem of interest.

The setting of this paper is a bit different. First, we are doing exploratory analysis, not predictive analysis. Second, while we do have labels which could be used to fine-tune the CNN (e.g. the PAM50 subtypes) we do not want to use these labels because then the network would be aware of information which we might want to (re)discover and/or validate in the following analysis. This leaves us with a couple of options to still use transfer learning including: training an unsupervised algorithm (e.g. auto-encoders Kingma and Welling (2013), generative adversarial networks Goodfellow et al. (2014) or self-supervised learning algorithms Oord, Li and Vinyals (2018); Lu et al. (2019)) or not doing any fine tuning. Ash et al. (2018) trains auto-encoder which has some disadvantages: a CNN is required to be trained which is time/resource consuming, a number of new hyper-parameters are introduced into the problem and either the data are used twice or external data are needed. We explore the latter option and show, perhaps surprisingly, that pre-trained CNN features with no fine tuning are able to capture complex visual signals in a domain vastly different than the one they were originally trained on.

Even in the context of transfer learning, there are many choices to be made about how to extract neural network features from an image including: network architecture, layer (or layers) of the network, and feature aggregation (e.g. spatial mean pooling discussed in Section 2.3). For predictive modeling these hyper-parameters can be set using an error metric and methods such as cross-validation, however, as discussed in the above paragraph, we do not have such error metrics readily available to guide hyper-parameter choices. Preliminary sensitivity analysis showed that the results of our analysis are not particularly sensitive to mild differences in architecture choices. Better methods to select these CNN hyper-parameters is an open area of research.

## APPENDIX A: APPENDIX SECTION

**A.1. Common tissue structures.** Below we give examples of some of the tissue structures which are relevant to this paper. Histopathology images are quite complex and pathologists are trained for years to interpret them.<sup>17</sup> For a more in-depth discussion of breast cancer pathology see Rosen (2001); Schnitt and Collins (2009).

<sup>16</sup>Passing the full core images through the CNN resulted in  $10^6$  features.

<sup>17</sup>And pathologists don't always agree with each other about their interpretations Elmore et al. (2015).

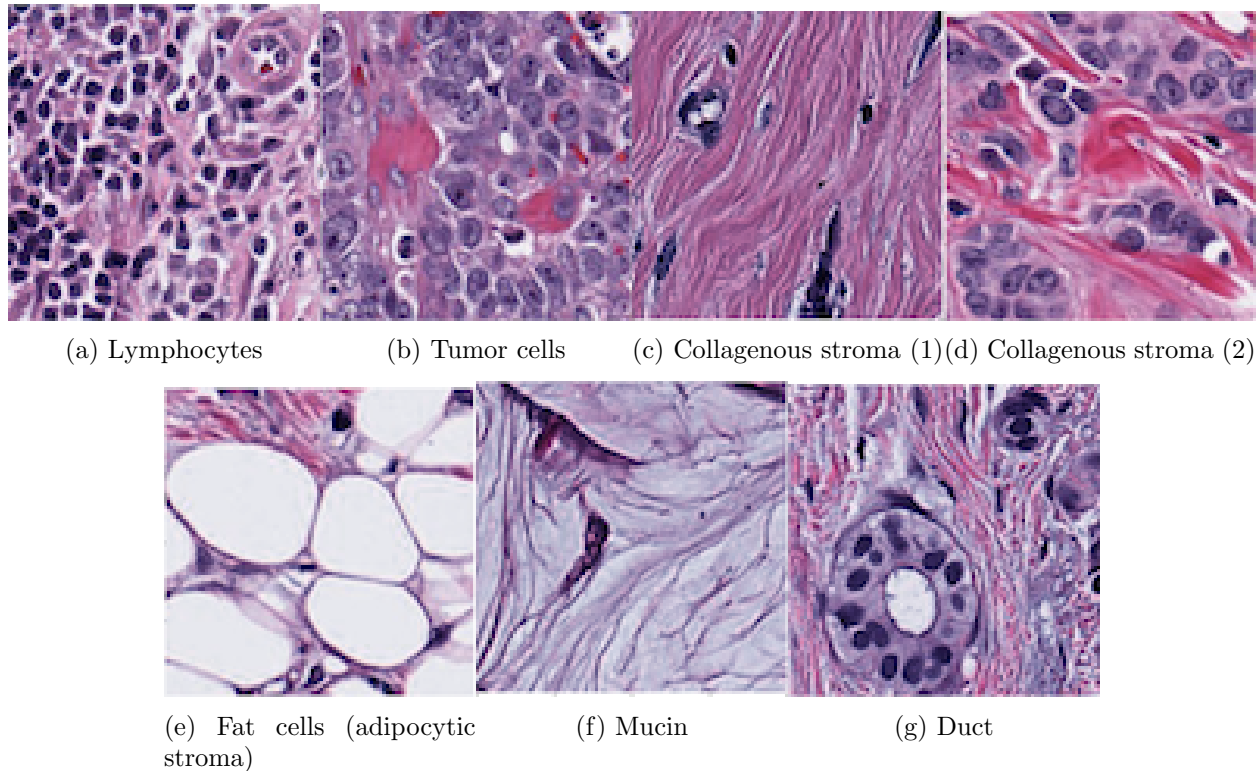


Fig 20: Examples of some of the common histology structures discussed in this paper.

- Figure 20a shows tumor infiltrating lymphocytes (TILs), the nuclei of which are basophilic (dark blue or purple) in conventional hematoxylin and eosin-stained (H&E) tissue sections. Hematoxylin quantitatively stains nucleic acids (DNA and RNA). Stromal TILs are more common in certain subtypes of breast cancer and may be associated with prognosis and response to treatment.
- Figure 20b shows mostly high nuclear grade tumor cells (basophilic, dark blue or purple nuclei on H&E) as well as some stroma (eosinophilic or pink on H&E). Nuclear grade describes how abnormal the tumor cells look: “low grade” means the nuclei resemble those of normal cells and “high grade” means the nuclei are enlarged, hyperchromatic (more basophilic, darker blue/purple staining than normal nuclei), irregularly shaped and may contain multiple nucleoli. Nucleoli are small intranuclear organelles that contain DNA, RNA and protein and are responsible for the synthesis of ribosomes (ribosomes are the organelles that synthesize proteins).
- Figure 20c shows collagenous stroma which is synthesized by fibroblasts and myofibroblasts and appears as eosinophilic (pink) fibrillar extracellular material on H&E. Collagenous stroma is the connective tissue that provides the scaffolding and support for epithelial structures. The nuclei (basophilic, dark blue or purple on H&E) of a few fibroblasts are visible in a collagenous stroma.
- Figure 20d shows clusters of tumor cells separated by areas of eosinophilic (pink) collagenous stroma. On H&E-stained tissue sections, the tumor cell nuclei and their contents are basophilic (blue/purple) and the tumor cell cytoplasm varies from pale to eosinophilic (pink). This is a common histologic appearance of breast cancer as it invades into the stroma as aggregates or sheets of tumor cells.

- The large white spaces in Figure 20e are the cytoplasm of adipocytes, cells that synthesize lipids (i.e, fat). The lipid-filled cytoplasm of adipocytes appears as these optically clear areas because the solvents used in the routine preparation of H&E tissue sections dissolve the lipids, leaving blank spaces where the lipids in the cytoplasm were. The ratio of fatty stroma to collagenous or fibrous stroma varies with age. Older patients will have more fatty stroma than younger patients. This age-related decrease in breast stromal density accounts for the increased accuracy of mammography in older patients.
- Figure 20f shows extracellular mucin, a glycoprotein produced by epithelial cells which can be present in both normal and tumor tissue. Mucin appears almost clear or pale pink or blue in H&E-stained tissue sections. Invasive breast cancers with pure mucinous histology are often low-grade and are thought to have a better prognosis than invasive ductal carcinoma of no special type.
- Figure 20g shows a normal duct in the lower left and low cellularity invasive carcinoma in the upper right part of the image. The benign cells contain nuclei that lack the enlargement, irregular shape and multiple nucleoli often seen in tumor cell nuclei. The benign cells have ample pale eosinophilic (pink) cytoplasm. The cells rest on a thin basement membrane which appears as a circumferential eosinophilic (pink) band around the periphery of the duct. The optically clear space in the middle of the duct is the lumen.

**REMARK A.1.** *There are a couple of terms important to this paper which are similar but have different meanings. Clinical HER2 and molecular HER2 are two separate classifications used in breast cancer; the former is a immunohistochemical classification used in the clinic to determine clinical decision making while the latter is a genetic subtype. High nuclear grade refers to individual cancer cells; high tumor grade is based on a composite index including nuclear grade, tubule formation and mitotic activity. Collagenous stroma refers to (the pink) connective tissue; adipocytic stroma refers to (the white) fat cells.*

**A.2. AJIVE diagnostics.** The initial signal ranks are 81 (image features) and 30 (genes). There were chosen by inspection of the the difference of the log-singular values and airing on the side of picking too high a rank.

Note the Wedin bound does not provide any value for these data. This is likely due to known conservativeness of the Wedin bound for non-square matrices. The random direction bound – which can be seen to be equivalent to the classical Roy’s latent root test for CCA rank selection – estimates the joint rank to be 7. This estimated joint rank was fairly robust to moderate changes in the initial signal ranks. The image individual rank is estimated to be 76 and genetic individual rank is estimated to be 25. These are likely overestimates, however, we focus only on the first few individual components.

**A.3. Clinical data interpretation methods.** In addition to the H&E images and gene expression data, we have a variety of clinical variables which can be used to interpret the different AJIVE components (e.g. PAM50 subtype). We compare each clinical variable of interest with the AJIVE scores for each component (i.e. the common normalized scores, image individual scores and genetic individual scores).

For continuous variables (e.g. proliferation score) we create a scatter plot, report the Pearson correlation and use the standard t-test test to determine if the association is statistically significant. For example, Figure 5c shows the first joint component (x-axis) compared to the proliferation scores (y-axis). The text in the top left reports the Pearson correlation and is bolded if the correlation is statistically significant (after correction for multiple testing).

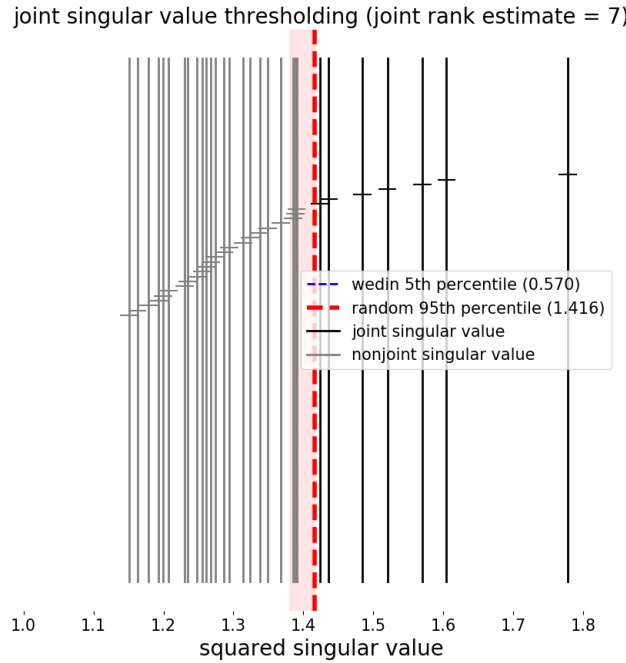


Fig 21: The AJIVE diagnostic plot shows that 7 possible joint directions are closer together than random. The vertical black/gray line segments show the principal angles between the  $X$  and  $Y$  signal subspaces (on the squared singular value scale). The vertical, red, shaded bar shows the 5-95th percentile of the distribution of leading principal angles between two random subspaces with the same dimensions as  $X$  and  $Y$ . The dashed, vertical, red line shows the random direction cutoff. The gray line segments correspond to angles larger than the cutoff while the black line segments correspond to the angles smaller than the cutoff.

For categorical variables we show a conditional histogram of the scores and report difference in distribution tests for each possible class comparison using the Mann Whitney U test. This test is used because it looks for location differences and because its test statistic is equivalent to the AUC statistic which gives an interpretable measure of how well separated two classes are. For categorical variables with more than 2 classes (e.g. there are five PAM50 subtypes) we do all one-vs-one comparisons.

For example, Figure 5b shows the first joint component (x-axis) conditioned on PAM50 subtype. The legend lists the classes, number of subjects in each class, and the the type of test. For a given class, the legend lists the other classes which were statistically significantly separated (after multiple testing adjustment) and reports the test statistics (AUC score) in parentheses. The class name is bold if at least one other class is statistically significantly separated. For example, in Figure 5b molecular Her2 is statistically significantly separated from Basal (AUC = 0.876), Luminal A (AUC = 0.897) and Normal (AUC = 0.827), but not Luminal B.

We compare each of the joint and individual AJIVE components to 33 variables. Additionally, for each multi-class categorical variable we do all of the one vs. one tests (e.g. for 5 classes we do  $\binom{5}{2}$  tests). Therefore adjustment for multiple testing is necessary to avoid spurious results. For each of the AJIVE joint, image individual and genetic individual components we use the Benjamini-Hochberg procedure [Benjamini and Hochberg \(1995\)](#) which is implemented in Statsmodels [Seabold and Perktold \(2010\)](#).

Some of the clinical variables (e.g. proliferation scores, PAM50 molecular subtype) compared to

the AJIVE scores are derived directly from the PAM50 gene expression which were used in the AJIVE analysis. This raises issues related to *post selection inference* when we compute p-values for these comparisons. Because the focus of this paper is on exploratory analysis we leave these issues for follow up work.

All joint, image individual and genetic individual clinical data comparisons are shown provided in [Supplement A](#).

#### ACKNOWLEDGEMENTS

We thank the Carolina Breast Cancer Study participants and staff. We also want to acknowledge Robert C. Millikan, founder of the Carolina Breast Cancer Study Phase 3. Research reported in this publication was supported by a Specialized Program of Research Excellence (SPORE) in breast cancer (P50 CA058223), an award from the Susan G. Komen Foundation (OGUNC1202), the North Carolina University Cancer Research Fund, and a Cancer Center Support Grant (P30 CA016086). Iain Carmichael and J. S. Marron were partially supported by NSF Grant IIS-1633074, BIG DATA 2016-2019. Iain Carmichael is currently supported by NSF MSPRF DMS-1902440. Katherine Hoadley was supported by Komen Career Catalyst Grant (CCR16376756).

#### SUPPLEMENTARY MATERIAL

##### Supplement A: Supplementary results

(<https://marronwebfiles.sites.oasis.unc.edu/AJIVE-Hist-Gene/>). Additional results and figures can be found in the zipped folder located at the above link (this file is large – approximately 1.5 Gb). These include all representative patch views shown to pathologists, all AJIVE genetic loadings vectors and all clinical data comparisons. See the file readme.txt for details.

#### REFERENCES

ABELS, E., PANTANOWITZ, L., AEFFNER, F., ZARELLA, M. D., VAN DER LAAK, J., BUI, M. M., VEMURI, V. N., PARWANI, A. V., GIBBS, J., AGOSTO-ARROYO, E. et al. (2019). Computational pathology definitions, best practices, and recommendations for regulatory guidance: a white paper from the Digital Pathology Association. *The Journal of pathology* **249** 286–294.

ADEBAYO, J., GILMER, J., MUELLY, M., GOODFELLOW, I., HARDT, M. and KIM, B. (2018). Sanity checks for saliency maps. In *Advances in Neural Information Processing Systems* 9505–9515.

AEFFNER, F., ZARELLA, M. D., BUCHBINDER, N., BUI, M. M., GOODMAN, M. R., HARTMAN, D. J., LUJAN, G. M., MOLANI, M. A., PARWANI, A. V., LILLARD, K. et al. (2019). Introduction to digital image analysis in whole-slide imaging: A white paper from the digital pathology association. *Journal of pathology informatics* **10**.

ALLOTT, E. H., GERADTS, J., COHEN, S. M., KHOURY, T., ZIRPOLI, G. R., BSHARA, W., DAVIS, W., OMILIAN, A., NAIR, P., ONDRACEK, R. P. et al. (2018). Frequency of breast cancer subtypes among African American women in the AMBER consortium. *Breast Cancer Research* **20** 12.

ASENDORF, N. A. (2015). Informative data fusion: Beyond canonical correlation analysis, PhD thesis, University of Michigan.

ASH, J., DARNELL, G., MUNRO, D. and ENGELHARDT, B. (2018). Joint analysis of gene expression levels and histological images identifies genes associated with tissue morphology. *bioRxiv* 458711.

BACKENROTH, D., GOLDSMITH, J., HARRAN, M. D., CORTES, J. C., KRAKAUER, J. W. and KITAGO, T. (2018). Modeling Motor Learning Using Heteroscedastic Functional Principal Components Analysis. *Journal of the American Statistical Association* **113** 1003–1015.

BECK, A. H., SANGOI, A. R., LEUNG, S., MARINELLI, R. J., NIELSEN, T. O., VAN DE VIJVER, M. J., WEST, R. B., VAN DE RIJN, M. and KOLLER, D. (2011). Systematic analysis of breast cancer morphology uncovers stromal features associated with survival. *Science translational medicine* **3** 108ra113–108ra113.

BEJNORDI, B. E., MULLOOLY, M., PFEIFFER, R. M., FAN, S., VACEK, P. M., WEAVER, D. L., HERSCHORN, S., BRINTON, L. A., VAN GINNEKEN, B., KARSSEMEIJER, N. et al. (2018). Using deep convolutional neural networks to identify and classify tumor-associated stroma in diagnostic breast biopsies. *Modern Pathology* **31** 1502.

BENGIO, Y., COURVILLE, A. and VINCENT, P. (2013). Representation learning: A review and new perspectives. *IEEE transactions on pattern analysis and machine intelligence* **35** 1798–1828.

BENJAMINI, Y. and HOCHBERG, Y. (1995). Controlling the false discovery rate: a practical and powerful approach to multiple testing. *Journal of the Royal statistical society: series B (Methodological)* **57** 289–300.

BISHOP, C. M. and TIPPING, M. E. (1998). A hierarchical latent variable model for data visualization. *IEEE Transactions on Pattern Analysis and Machine Intelligence* **20** 281–293.

CALDARELLA, A., BUZZONI, C., CROCETTI, E., BIANCHI, S., VEZZOSI, V., APICELLA, P., BIANCALANI, M., GIANNINI, A., URSO, C., ZOLFANELLI, F. et al. (2013). Invasive breast cancer: a significant correlation between histological types and molecular subgroups. *Journal of cancer research and clinical oncology* **139** 617–623.

CARMICHAEL, I. (2019). PyJive: an python library implementing AJIVE. [https://github.com/idc9/py\\_jive](https://github.com/idc9/py_jive).

CHEN, C., LI, O., TAO, C., BARNETT, A. J., SU, J. and RUDIN, C. (2018a). This looks like that: deep learning for interpretable image recognition. *arXiv preprint arXiv:1806.10574*.

CHEN, P.-H. C., GADEPALLI, K., MACDONALD, R., LIU, Y., NAGPAL, K., KOHLBERGER, T., DEAN, J., CORRADO, G. S., HIPP, J. D. and STUMPE, M. C. (2018b). Microscope 2.0: an augmented reality microscope with real-time artificial intelligence integration. *arXiv preprint arXiv:1812.00825*.

CHOLLET-HINTON, L., PUUVANESARAJAH, S., SANDHU, R., KIRK, E. L., MIDKIFF, B. R., GHOSH, K., BRANDT, K. R., SCOTT, C. G., GIERACH, G. L., SHERMAN, M. E. et al. (2018). Stroma modifies relationships between risk factor exposure and age-related epithelial involution in benign breast. *Modern Pathology* **31** 1085.

COLLEONI, M., ROTMENSZ, N., MAISONNEUVE, P., MASTROPASQUA, M., LUINI, A., VERONESI, P., INTRA, M., MONTAGNA, E., CANCELLO, G., CARDILLO, A. et al. (2011). Outcome of special types of luminal breast cancer. *Annals of oncology* **23** 1428–1436.

COOPER, L. A., KONG, J., GUTMAN, D. A., DUNN, W. D., NALISNIK, M. and BRAT, D. J. (2015). Novel genotype-phenotype associations in human cancers enabled by advanced molecular platforms and computational analysis of whole slide images. *Laboratory investigation* **95** 366.

COUTURE, H. D., WILLIAMS, L. A., GERADTS, J., NYANTE, S. J., BUTLER, E. N., MARRON, J. S., PEROU, C. M., TROESTER, M. A. and NIETHAMMER, M. (2018). Image analysis with deep learning to predict breast cancer grade, ER status, histologic subtype, and intrinsic subtype. *NPJ breast cancer* **4** 30.

DENG, J., DONG, W., SOCHER, R., LI, L.-J., LI, K. and FEI-FEI, L. (2009). Imagenet: A large-scale hierarchical image database. In *2009 IEEE conference on computer vision and pattern recognition* 248–255. Ieee.

DI SAVERIO, S., GUTIERREZ, J. and AVISAR, E. (2008). A retrospective review with long term follow up of 11,400 cases of pure mucinous breast carcinoma. *Breast cancer research and treatment* **111** 541–547.

DIAB, S. G., CLARK, G. M., OSBORNE, C. K., LIBBY, A., ALLRED, D. C. and ELLEDGE, R. M. (1999). Tumor characteristics and clinical outcome of tubular and mucinous breast carcinomas. *Journal of clinical oncology* **17** 1442–1442.

DOSHI-VELEZ, F. and KIM, B. (2017). Towards a rigorous science of interpretable machine learning. *arXiv preprint arXiv:1702.08608*.

DRAPER, B., KIRBY, M., MARKS, J., MARRINAN, T. and PETERSON, C. (2014). A flag representation for finite collections of subspaces of mixed dimensions. *Linear Algebra and its Applications* **451** 15–32.

EIRO, N., GONZALEZ, L. O., FRAILE, M., CID, S., SCHNEIDER, J. and VIZOSO, F. J. (2019). Breast cancer tumor stroma: cellular components, phenotypic heterogeneity, intercellular communication, prognostic implications and therapeutic opportunities. *Cancers* **11** 664.

ELMORE, J. G., LONGTON, G. M., CARNEY, P. A., GELLER, B. M., ONEGA, T., TOSTESON, A. N., NELSON, H. D., PEPE, M. S., ALLISON, K. H., SCHNITT, S. J. et al. (2015). Diagnostic concordance among pathologists interpreting breast biopsy specimens. *Jama* **313** 1122–1132.

ELSTON, C. W. and ELLIS, I. O. (2002). Pathological prognostic factors in breast cancer. I. The value of histological grade in breast cancer: experience from a large study with long-term follow-up. CW Elston & IO Ellis. Histopathology 1991; 19; 403–410: AUTHOR COMMENTARY. *Histopathology* **41** 151–151.

FENG, Q., JIANG, M., HANNIG, J. and MARRON, J. (2018). Angle-based joint and individual variation explained. *Journal of multivariate analysis* **166** 241–265.

FUKUSHIMA, K. (1980). Neocognitron: A self-organizing neural network model for a mechanism of pattern recognition unaffected by shift in position. *Biological cybernetics* **36** 193–202.

GAYANOVA, I. and LI, G. (2017). Structural learning and integrative decomposition of multi-view data. *arXiv preprint arXiv:1707.06573*.

GOODFELLOW, I., POUGET-ABADIE, J., MIRZA, M., XU, B., WARDE-FARLEY, D., OZAIR, S., COURVILLE, A. and BENGIO, Y. (2014). Generative adversarial nets. In *Advances in neural information processing systems* 2672–2680.

GYÓRFFY, B., HATZIS, C., SANFT, T., HOFSTATTER, E., AKTAS, B. and PUSZTAI, L. (2015). Multigene prognostic tests in breast cancer: past, present, future. *Breast cancer research* **17** 11.

HENG, Y. J., LESTER, S. C., TSE, G. M., FACTOR, R. E., ALLISON, K. H., COLLINS, L. C., CHEN, Y.-Y., JENSEN, K. C., JOHNSON, N. B., JEONG, J. C. et al. (2017). The molecular basis of breast cancer pathological phenotypes. *The Journal of pathology* **241** 375–391.

HOLZINGER, A., LANGS, G., DENK, H., ZATLOUKAL, K. and MÜLLER, H. (2019). Causability and explainability of

artificial intelligence in medicine. *Wiley Interdisciplinary Reviews: Data Mining and Knowledge Discovery* e1312.

HOTELLING, H. (1936). Relation between two sets of variates. *Biometrika*.

HUNTER, J. D. (2007). Matplotlib: A 2D graphics environment. *Computing in science & engineering* **9** 90.

ILSE, M., TOMCZAK, J. M. and WELLING, M. (2018). Attention-based deep multiple instance learning. *arXiv preprint arXiv:1802.04712*.

JIMÉNEZ, G. and RACOCEANU, D. (2019). Deep Learning for Semantic Segmentation versus Classification in Computational Pathology: Application to mitosis analysis in Breast Cancer grading. *Frontiers in Bioengineering and Biotechnology* **7** 145.

JOHNSTONE, I. M. (2008). Multivariate analysis and Jacobi ensembles: Largest eigenvalue, Tracy–Widom limits and rates of convergence. *Annals of statistics* **36** 2638.

JONES, E., OLIPHANT, T. and PETERSON, P. (2014). SciPy: Open source scientific tools for Python.

KETTENRING, J. R. (1971). Canonical analysis of several sets of variables. *Biometrika* **58** 433–451.

KIM, B., WATTENBERG, M., GILMER, J., CAI, C., WEXLER, J., VIEGAS, F. et al. (2018). Interpretability Beyond Feature Attribution: Quantitative Testing with Concept Activation Vectors (TCAV). In *International Conference on Machine Learning* 2673–2682.

KINGMA, D. P. and WELLING, M. (2013). Auto-encoding variational bayes. *arXiv preprint arXiv:1312.6114*.

KOMURA, D. and ISHIKAWA, S. (2018). Machine learning methods for histopathological image analysis. *Computational and structural biotechnology journal* **16** 34–42.

LACROIX-TRIKI, M., SUAREZ, P. H., MACKAY, A., LAMBROS, M. B., NATRAJAN, R., SAVAGE, K., GEYER, F. C., WEIGELT, B., ASHWORTH, A. and REIS-FILHO, J. S. (2010). Mucinous carcinoma of the breast is genetically distinct from invasive ductal carcinomas of no special type. *The Journal of pathology* **222** 282–298.

LAZARD, D., SASTRE, X., FRID, M. G., GLUKHOVA, M. A., THIERY, J.-P. and KOTELIANSKY, V. E. (1993). Expression of smooth muscle-specific proteins in myoepithelium and stromal myofibroblasts of normal and malignant human breast tissue. *Proceedings of the National Academy of Sciences* **90** 999–1003.

LECUN, Y., BENGIO, Y. and HINTON, G. (2015). Deep learning. *nature* **521** 436.

LIU, Y., GADEPALLI, K., NOROUZI, M., DAHL, G. E., KOHLBERGER, T., BOYKO, A., VENUGOPALAN, S., TIMOFEEV, A., NELSON, P. Q., CORRADO, G. S. et al. (2017). Detecting cancer metastases on gigapixel pathology images. *arXiv preprint arXiv:1703.02442*.

LIU, Y., KOHLBERGER, T., NOROUZI, M., DAHL, G. E., SMITH, J. L., MOHTASHAMIAN, A., OLSON, N., PENG, L. H., HIPP, J. D. and STUMPE, M. C. (2018). Artificial Intelligence-Based Breast Cancer Nodal Metastasis Detection: Insights Into the Black Box for Pathologists. *Archives of pathology & laboratory medicine*.

LIVASY, C. A., KARACA, G., NANDA, R., TRETIAKOVA, M. S., OLOPADE, O. I., MOORE, D. T. and PEROU, C. M. (2006). Phenotypic evaluation of the basal-like subtype of invasive breast carcinoma. *Modern pathology* **19** 264.

LOCK, E. F., HOADLEY, K. A., MARRON, J. S. and NOBEL, A. B. (2013). Joint and individual variation explained (JIVE) for integrated analysis of multiple data types. *The annals of applied statistics* **7** 523.

LU, M. Y., CHEN, R. J., WANG, J., DILLON, D. and MAHMOOD, F. (2019). Semi-Supervised Histology Classification using Deep Multiple Instance Learning and Contrastive Predictive Coding. *arXiv preprint arXiv:1910.10825*.

MACENKO, M., NIETHAMMER, M., MARRON, J. S., BORLAND, D., WOOSLEY, J. T., GUAN, X., SCHMITT, C. and THOMAS, N. E. (2009). A method for normalizing histology slides for quantitative analysis. In *2009 IEEE International Symposium on Biomedical Imaging: From Nano to Macro* 1107–1110. IEEE.

MAHMOOD, F., YANG, Z., ASHLEY, T. and DURR, N. J. (2018). Multimodal densenet. *arXiv preprint arXiv:1811.07407*.

MAHMOOD, F., BORDERS, D., CHEN, R., MCKAY, G. N., SALIMIAN, K. J., BARAS, A. and DURR, N. J. (2019). Deep adversarial training for multi-organ nuclei segmentation in histopathology images. *IEEE transactions on medical imaging*.

MARRON, J. S. and ALONSO, A. M. (2014). Overview of object oriented data analysis. *Biometrical Journal* **56** 732–753.

McKINNEY, W. (2011). Pandas: a foundational Python library for data analysis and statistics. *Python for High Performance and Scientific Computing* **14**.

MOLNAR, C. et al. (2018). Interpretable machine learning: A guide for making black box models explainable. *E-book at <https://christophm.github.io/interpretable-ml-book/>, version dated 10*.

NETWORK, C. G. A. et al. (2012). Comprehensive molecular portraits of human breast tumours. *Nature* **490** 61.

NIAZI, M. K. K., PARWANI, A. V. and GURCAN, M. N. (2019). Digital pathology and artificial intelligence. *The Lancet Oncology* **20** e253–e261.

NIELSEN, A. A. (2002). Multiset canonical correlations analysis and multispectral, truly multitemporal remote sensing data. *IEEE transactions on image processing* **11** 293–305.

OH, D. S., TROESTER, M. A., USARY, J., HU, Z., HE, X., FAN, C., WU, J., CAREY, L. A. and PEROU, C. M. (2006). Estrogen-regulated genes predict survival in hormone receptor-positive breast cancers. *J Clin Oncol* **24** 1656–1664.

OLAH, C., SATYANARAYAN, A., JOHNSON, I., CARTER, S., SCHUBERT, L., YE, K. and MORDVINTSEV, A. (2018). The building blocks of interpretability. *Distill* **3** e10.

OORD, A. v. d., LI, Y. and VINYALS, O. (2018). Representation learning with contrastive predictive coding. *arXiv preprint arXiv:1807.03748*.

OTSU, N. (1979). A threshold selection method from gray-level histograms. *IEEE transactions on systems, man, and cybernetics* **9** 62–66.

PARKER, J. S., MULLINS, M., CHEANG, M. C., LEUNG, S., VODUC, D., VICKERY, T., DAVIES, S., FAURON, C., HE, X., HU, Z. et al. (2009). Supervised risk predictor of breast cancer based on intrinsic subtypes. *Journal of clinical oncology* **27** 1160.

PASZKE, A., GROSS, S., CHINTALA, S., CHANAN, G., YANG, E., DEVITO, Z., LIN, Z., DESMAISON, A., ANTIGA, L. and LERER, A. (2017). Automatic differentiation in pytorch.

PEDREGOSA, F., VAROQUAUX, G., GRAMFORT, A., MICHEL, V., THIRION, B., GRISEL, O., BLONDEL, M., PRETTENHOFER, P., WEISS, R., DUBOURG, V., VANDERPLAS, J., PASSOS, A., COURNAPEAU, D., BRUCHER, M., PERROT, M. and DUCHESNAY, E. (2011). Scikit-learn: Machine Learning in Python. *Journal of Machine Learning Research* **12** 2825–2830.

PEROU, C. M., SØRLIE, T., EISEN, M. B., VAN DE RIJN, M., JEFFREY, S. S., REES, C. A., POLLACK, J. R., ROSS, D. T., JOHNSEN, H., AKSLEN, L. A. et al. (2000). Molecular portraits of human breast tumours. *nature* **406** 747.

POURZANJANI, A. A., WU, T. B., JIANG, R. M., COHEN, M. J. and PETZOLD, L. R. (2017). Understanding Coagulopathy using Multi-view Data in the Presence of Sub-Cohorts: A Hierarchical Subspace Approach. In *Machine Learning for Healthcare Conference* 338–351.

ROMÁN-PÉREZ, E., CASBAS-HERNÁNDEZ, P., PIRONE, J. R., REIN, J., CAREY, L. A., LUBET, R. A., MANI, S. A., AMOS, K. D. and TROESTER, M. A. (2012). Gene expression in extratumoral microenvironment predicts clinical outcome in breast cancer patients. *Breast Cancer Research* **14** R51.

ROSEN, P. P. (2001). *Rosen's breast pathology*. Lippincott Williams & Wilkins.

SCHNITT, S. J. and COLLINS, L. C. (2009). *Biopsy interpretation of the breast*. Lippincott Williams & Wilkins.

SEABOLD, S. and PERKTOLD, J. (2010). Statsmodels: Econometric and statistical modeling with python. In *Proceedings of the 9th Python in Science Conference* **57** 61. Scipy.

SELVARAJU, R. R., COGSWELL, M., DAS, A., VEDANTAM, R., PARikh, D. and BATRA, D. (2017). Grad-cam: Visual explanations from deep networks via gradient-based localization. In *2017 IEEE International Conference on Computer Vision (ICCV)* 618–626. IEEE.

SHARIF RAZAVIAN, A., AZIZPOUR, H., SULLIVAN, J. and CARLSSON, S. (2014). CNN features off-the-shelf: an astounding baseline for recognition. In *Proceedings of the IEEE conference on computer vision and pattern recognition workshops* 806–813.

SIMONYAN, K. and ZISSERMAN, A. (2014). Very deep convolutional networks for large-scale image recognition. *arXiv preprint arXiv:1409.1556*.

SPRINGENBERG, J. T., DOSOVITSKIY, A., BROX, T. and RIEDMILLER, M. (2014). Striving for simplicity: The all convolutional net. *arXiv preprint arXiv:1412.6806*.

SRIVASTAVA, A., KULKARNI, C., MALLICK, P., HUANG, K. and MACHIRAJU, R. (2018). Building trans-omics evidence: using imaging and'omics' to characterize cancer profiles. In *PSB* 377–388. World Scientific.

SUNDARARAJAN, M., TALY, A. and YAN, Q. (2017). Axiomatic attribution for deep networks. In *Proceedings of the 34th International Conference on Machine Learning-Volume 70* 3319–3328. JMLR.org.

TITFORD, M. (2006). A short history of histopathology technique. *Journal of Histotechnology* **29** 99–110.

TROESTER, M. A., SUN, X., ALLOTT, E. H., GERADTS, J., COHEN, S. M., TSE, C.-K., KIRK, E. L., THORNE, L. B., MATHEWS, M., LI, Y. et al. (2017). Racial differences in PAM50 subtypes in the Carolina Breast Cancer Study. *JNCI: Journal of the National Cancer Institute* **110** 176–182.

VAN DER WALT, S., COLBERT, S. C. and VAROQUAUX, G. (2011). The NumPy array: a structure for efficient numerical computation. *Computing in Science & Engineering* **13** 22.

VAN DER WALT, S., SCHÖNBERGER, J. L., NUNEZ-IGLESIAS, J., BOULOGNE, F., WARNER, J. D., YAGER, N., GOUIL-LART, E. and YU, T. (2014). scikit-image: image processing in Python. *PeerJ* **2** e453.

VELLIDO, A., MARTÍN-GUERRERO, J. D. and LISBOA, P. J. (2012). Making machine learning models interpretable. In *ESANN* **12** 163–172. Citeseer.

VETA, M., HENG, Y. J., STATHONIKOS, N., BEJNORDI, B. E., BECA, F., WOLLMANN, T., ROHR, K., SHAH, M. A., WANG, D., ROUSSON, M. et al. (2019). Predicting breast tumor proliferation from whole-slide images: the TUPAC16 challenge. *Medical Image Analysis*.

WANG, C., PÉCOT, T., ZYNGER, D. L., MACHIRAJU, R., SHAPIRO, C. L. and HUANG, K. (2013). Identifying survival associated morphological features of triple negative breast cancer using multiple datasets. *Journal of the American Medical Informatics Association* **20** 680–687.

WANG, D., KHOSLA, A., GARGEYA, R., IRSHAD, H. and BECK, A. H. (2016). Deep learning for identifying metastatic

breast cancer. *arXiv preprint arXiv:1606.05718*.

WASKOM, M., BOTVINNIK, O., O'KANE, D., HOBSON, P., OSTBLOM, J., LUKAUSKAS, S., GEMPERLINE, D. C., AUGSPURGER, T., HALCHENKO, Y., COLE, J. B., WARMENHOVEN, J., DE RUITER, J., PYE, C., HOYER, S., VANDERPLAS, J., VILLALBA, S., KUNTER, G., QUINTERO, E., BACHANT, P., MARTIN, M., MEYER, K., MILES, A., RAM, Y., BRUNNER, T., YARKONI, T., WILLIAMS, M. L., EVANS, C., FITZGERALD, C., BRIAN and QALIEH, A. (2018). Seaborn (v0.9.0).

WEIGELT, B., GEYER, F. C., HORLINGS, H. M., KREIKE, B., HALFWERK, H. and REIS-FILHO, J. S. (2009). Mucinous and neuroendocrine breast carcinomas are transcriptionally distinct from invasive ductal carcinomas of no special type. *Modern Pathology* **22** 1401.

WEIN, L., SAVAS, P., LUEN, S. J., VIRASSAMY, B., SALGADO, R. and LOI, S. (2017). Clinical validity and utility of tumor-infiltrating lymphocytes in routine clinical practice for breast cancer patients: current and future directions. *Frontiers in oncology* **7** 156.

WHITFIELD, M. L., SHERLOCK, G., SALDANHA, A. J., MURRAY, J. I., BALL, C. A., ALEXANDER, K. E., MATESE, J. C., PEROU, C. M., HURT, M. M., BROWN, P. O. et al. (2002). Identification of genes periodically expressed in the human cell cycle and their expression in tumors. *Molecular biology of the cell* **13** 1977–2000.

WILLIAMS, L. A., HOADLEY, K. A., NICHOLS, H. B., GERADTS, J., PEROU, C. M., LOVE, M. I., OLSHAM, A. F. and TROESTER, M. A. (2019). Differences in race, molecular and tumor characteristics among women diagnosed with invasive ductal and lobular breast carcinomas. *Cancer Causes & Control* **30** 31–39.

WOLD, H. (1985). Partial least squares. S. Kotz and NL Johnson (Eds.), Encyclopedia of statistical sciences (vol. 6).

YANG, Z. and MICHAILIDIS, G. (2015). A non-negative matrix factorization method for detecting modules in heterogeneous omics multi-modal data. *Bioinformatics* **32** 1–8.

YOSINSKI, J., CLUNE, J., BENGIO, Y. and LIPSON, H. (2014). How transferable are features in deep neural networks? In *Advances in neural information processing systems* 3320–3328.

ZACK, G., ROGERS, W. and LATT, S. (1977). Automatic measurement of sister chromatid exchange frequency. *Journal of Histochemistry & Cytochemistry* **25** 741–753.

ZEILER, M. D. and FERGUS, R. (2014). Visualizing and understanding convolutional networks. In *European conference on computer vision* 818–833. Springer.

ZHAO, S., GAO, C., MUKHERJEE, S. and ENGELHARDT, B. E. (2014). Bayesian group latent factor analysis with structured sparsity. *arXiv preprint arXiv:1411.2698*.

I. CARMICHAEL  
DEPARTMENT OF STATISTICS  
UNIVERSITY OF WASHINGTON  
SEATTLE, WA, 98195  
[idc9@uw.edu](mailto:idc9@uw.edu)

K.A. HOADLEY  
DEPARTMENT OF GENETICS  
LINEBERGER COMPREHENSIVE CANCER CENTER  
COMPUTATIONAL MEDICINE PROGRAM  
UNIVERSITY OF NORTH CAROLINA AT CHAPEL HILL  
CHAPEL HILL, NC, 27599  
[hoadley@med.unc.edu](mailto:hoadley@med.unc.edu)

J. GERADTS  
DEPARTMENT OF POPULATION SCIENCES  
CITY OF HOPE NATIONAL MEDICAL CENTER  
DUARTE, CA 91010  
[jgeradts@coh.org](mailto:jgeradts@coh.org)

L. OLSSON  
DEPARTMENT OF EPIDEMIOLOGY  
UNIVERSITY OF NORTH CAROLINA AT CHAPEL HILL  
CHAPEL HILL, NC, 27599  
[lolsson@live.unc.edu](mailto:lolsson@live.unc.edu)

M. NIETHAMMER  
DEPARTMENT OF COMPUTER SCIENCE  
UNIVERSITY OF NORTH CAROLINA AT CHAPEL HILL  
CHAPEL HILL, NC, 27599  
[mn@cs.unc.edu](mailto:mn@cs.unc.edu)

B.C. CALHOUN  
DEPARTMENT OF PATHOLOGY AND LABORATORY MEDICINE  
UNIVERSITY OF NORTH CAROLINA AT CHAPEL HILL  
CHAPEL HILL, NC, 27599  
[ben.calhoun@unchealth.unc.edu](mailto:ben.calhoun@unchealth.unc.edu)

M.A. TROESTER  
DEPARTMENT OF EPIDEMIOLOGY  
DEPARTMENT OF PATHOLOGY AND LABORATORY MEDICINE  
UNIVERSITY OF NORTH CAROLINA AT CHAPEL HILL  
CHAPEL HILL, NC, 27599  
[troester@unc.edu](mailto:troester@unc.edu)

H.D. COUTURE  
PIXEL SCIENTIA LABS  
RALEIGH, NC, 27615  
[heather@pixelscientia.com](mailto:heather@pixelscientia.com)

C.M. PEROU  
DEPARTMENT OF GENETICS  
DEPARTMENT OF PATHOLOGY AND LABORATORY MEDICINE  
UNIVERSITY OF NORTH CAROLINA AT CHAPEL HILL  
CHAPEL HILL, NC, 27599  
[cperou@med.unc.edu](mailto:cperou@med.unc.edu)

J. HANNIG  
DEPARTMENT OF STATISTICS  
UNIVERSITY OF NORTH CAROLINA AT CHAPEL HILL  
CHAPEL HILL, NC, 27599  
[jan.hannig@unc.edu](mailto:jan.hannig@unc.edu)

J.S. MARRON  
DEPARTMENT OF STATISTICS  
UNIVERSITY OF NORTH CAROLINA AT CHAPEL HILL  
CHAPEL HILL, NC, 27599  
[marron@unc.edu](mailto:marron@unc.edu)